

1995

Software modeling for flaw characterization of metals through eddy-currents

Radhika Satveli
Iowa State University

Follow this and additional works at: <https://lib.dr.iastate.edu/rtd>

 Part of the [Computer Engineering Commons](#)

Recommended Citation

Satveli, Radhika, "Software modeling for flaw characterization of metals through eddy-currents" (1995). *Retrospective Theses and Dissertations*. 258.
<https://lib.dr.iastate.edu/rtd/258>

This Thesis is brought to you for free and open access by the Iowa State University Capstones, Theses and Dissertations at Iowa State University Digital Repository. It has been accepted for inclusion in Retrospective Theses and Dissertations by an authorized administrator of Iowa State University Digital Repository. For more information, please contact digirep@iastate.edu.

Software modeling for flaw characterization
of metals through eddy-currents

by

Radhika Satveli

A Thesis Submitted to the
Graduate Faculty in Partial Fulfillment of the
Requirements for the Degree of
MASTER OF SCIENCE

Department: Electrical and Computer Engineering
Major: Computer Engineering

Approved:

Members of the Committee:

Satish Udpa
In Charge of Major Work

James H. Rose

For the Major Department

S.K. Gadia

For the Graduate College

Iowa State University
Ames, Iowa

1995

Copyright © Radhika Satveli, 1995. All rights reserved.

TABLE OF CONTENTS

	Page
1. INTRODUCTION	1
2. ELECTRIC FIELD CALCULATION	9
3. RECIPROCITY-BASED FORMULA FOR CHANGE IN IMPEDANCE	22
4. PERTURBATION THEORY	29
5. THE BENCHMARK PROBLEM	33
6. PERTURBATION RESULTS FOR VARIOUS CANONICAL PROBLEMS	46
7. SUMMARY AND CONCLUSIONS	72
REFERENCES	73
ACKNOWLEDGMENTS	75

1. INTRODUCTION

1.1 Non Destructive Evaluation

Nondestructive evaluation (NDE) consists of methods and techniques for the periodic testing of materials and structures that do not require machine disassembly. Electromagnetic NDE makes use of electromagnetic induction, fields, or varying currents for probing and measuring the test samples and thus achieving NDE goals. The electromagnetic NDE cycle is as depicted in Figure 1.1. Eddy current NDE falls in the category of electromagnetic NDE.

1.2 Eddy Current NDE

1.2.1 Overview

Eddy current NDE follows the same path as the electromagnetic NDE and makes use of eddy currents for flaw characterization as shown in Figure 1.2. It is typically carried out through an eddy current probe driven by a time harmonic current source. A schematic picture is shown in Figure 1.3. The current probe is a coil of wire (wound in air or around a ferrite core) placed next to a metal structure that needs to be tested. The time varying magnetic flux of the probe induces eddy currents in the metal structure. If a flaw is present it will disturb the flow of eddy currents due to changes in electrical and magnetic properties in the region of the flaw. The changes indirectly register as changes in the probe's impedance and can be measured. This change in impedance depends on the structure of the flaw and can therefore be used for flaw characterization. Defect determination is divided into two problems:

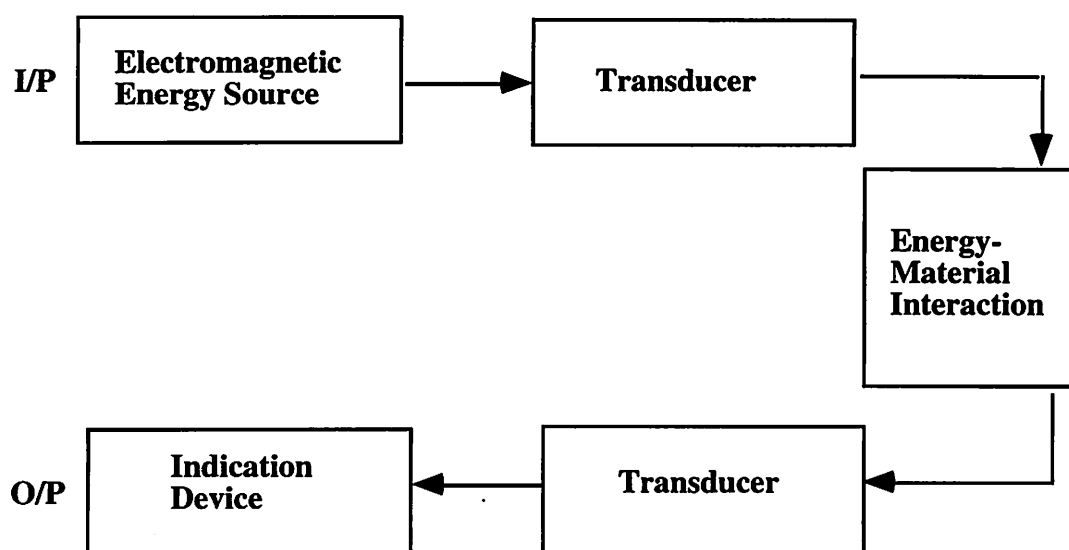


Figure 1.1: Electromagnetic non destructive evaluation cycle

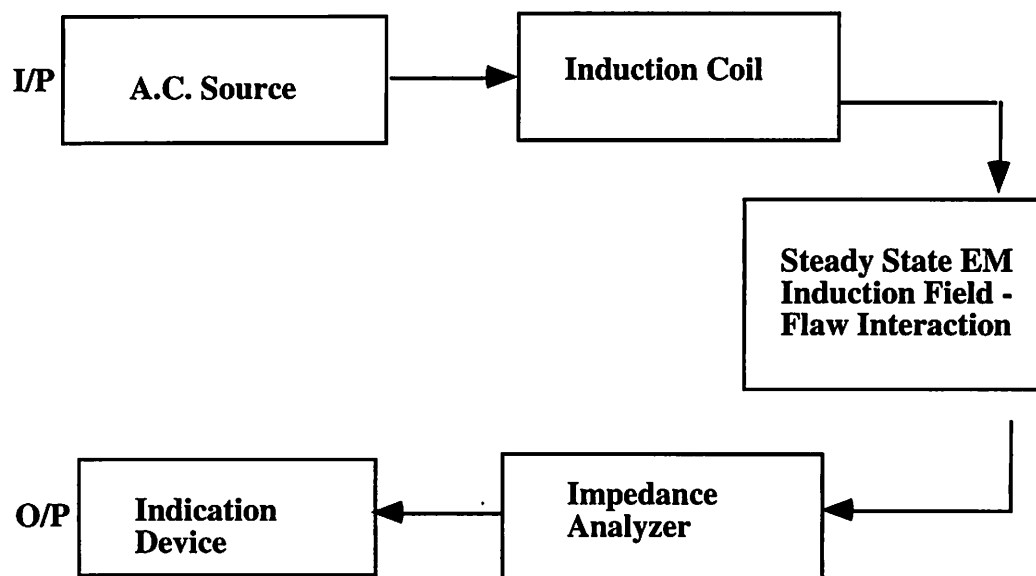


Figure 1.2: Eddy-current non destructive evaluation cycle

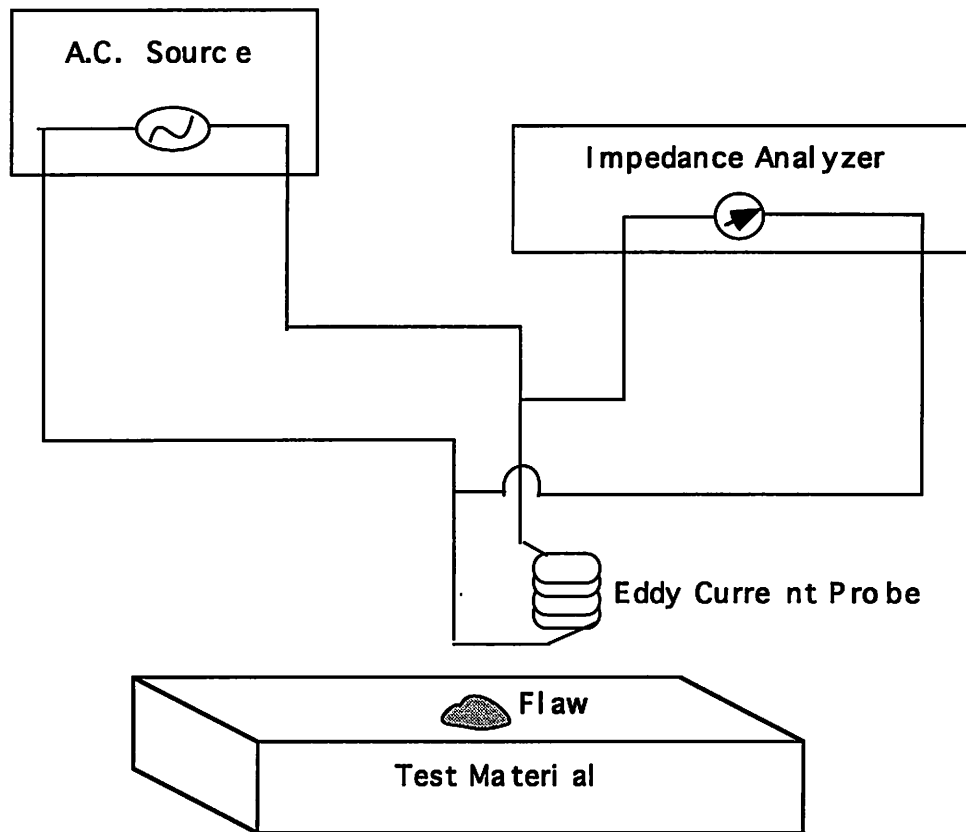


Figure 1.3: Schematic diagram of an eddy current setup for NDE

the forward problem and the inverse problem. The forward problem deals with prediction of the impedance change, given the defect dimensions. The inverse problem is to characterize the defect, given the change of impedance of the probe over a frequency range. This problem is more indirect. A possible solution would be to solve the forward problem for various defect dimensions and tabulate the results. Next compare the change in impedance obtained through actual measurement of the defective sample with the forward problem results. A match might indicate the dimensions of the defect.

Flaw characterization using practical measurements has existed for almost half a century but quantitative defect characterization using theoretical eddy-current models is fairly recent and potentially has a wide range of application in science and engineering. The inspection of layered metals for defects, which is the conductor geometry used in this thesis, is an important maintenance and quality control problem for industry. For example, the remaining life of the current US Air Force transport fleet is believed to be limited by hidden corrosion in the skin at lap-slices, which consist of two parallel plates of aluminum joined by rivets.

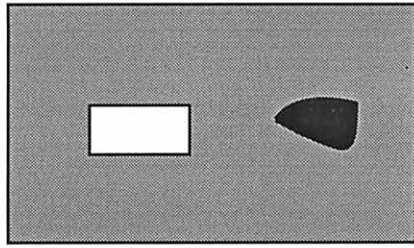
The impedance of a right-cylindrical air-core coil placed next to a layered metal can be accurately modeled by analytic formulas as long as the conductivity varies one-dimensionally with depth into the metal. No analytic solution is known to exist if a volumetric defect, due for example to localized pitting corrosion, breaks the one-dimensional symmetry. Numerically intensive calculations can be carried out for the resulting three-dimensional problem using for example finite-element or volume element methods. These calculations although possible are very demanding, time-consuming and often specialized to the solution of particular problems.

This thesis develops a new theoretical method for solving the forward eddy current problem based on perturbation theory. Perturbation methods are often used to provide solutions to physical problems whose solutions are otherwise too difficult or time-consuming.

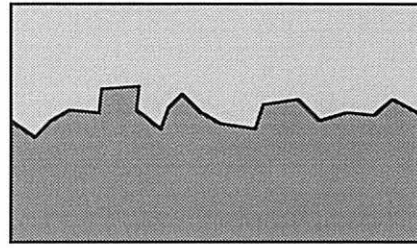
Although approximate, perturbative solutions are generally much simpler and less time-consuming than more exact approaches. The new perturbation method developed in this thesis is fairly general and can handle a wide range of NDE applications including characterization of regular and irregular defects, corrosion abnormalities, boundary deformations due to welding, forging etc., bolt or rivet size determination, determination of volume variation in properties and layer thickness determination in structures such as galvanized plates etc. (Figure 1.4). The new perturbation method was implemented in a software package, which was used to explore some of the problems just mentioned. The new perturbation model was tested by comparison to experimental results and also other existing theoretical models.

1.2.2 Background

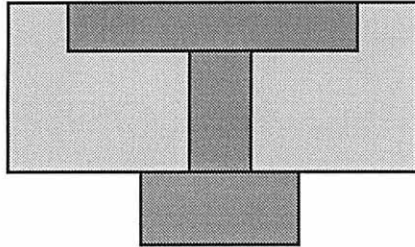
Eddy current testing has been used in industry for many years. The idea initiated from the use of induction coil to sort metals [1]. Eddy current testing was first introduced by Foster [2]. Theoretical eddy current modeling was first attempted by Burrows [3] and Dodd and Deeds [4]. Burrows developed flaw scattering equations from static Maxwell's equations at low frequencies. He introduced a low-frequency perturbative method for ellipsoidal inclusions in a metallic half-space. Cheng, Dodd and Deeds [5] extended Burrows method to ellipsoidal inclusions in arbitrarily layered metal sheets and cylindrical tubes. Theoretical modeling for metal layers with constant conductivities was considered by Norton and Khan [6] for cylindrical geometries and was later extended to planar geometries by Moulder, Uzal and Rose [7]. Uzal et. al considered samples in which the conductivity varied continuously. These methods were aimed at calculating the change in impedance directly. Burrow's approximation [3] gives the change in impedance in terms of electromagnetic fields in the conductor geometry. Auld developed an exact reciprocity-based formalism for the change in the eddy-current impedance. This formalism predicts the change in the impedance if the exact



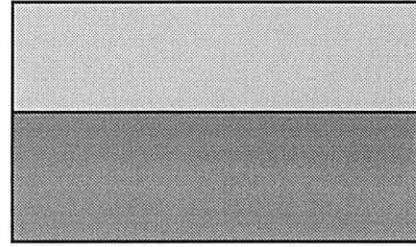
Regular and Irregular Defects



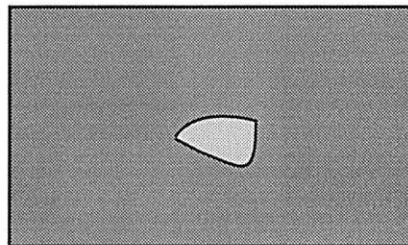
Corrosion and Boundary Deformations



Rivet Size Determination



Layer Thickness Determination



Volume Variation in Properties

Figure 1.4: Some industrial applications of flaw characterization using eddy current NDE that can be accomplished by the developed model.

electric field in the region (support) of the defect is known. Since, in general, the electric field in the region of defect cannot be exactly determined, various approximations for the electric field have been developed. One such approximation is the Born approximation [9]. Nair and Rose combined the Born approximation and Auld's reciprocity formula to treat both the forward and inverse problem for volumetric defects [10]. More recently, the Born approximation was developed directly in terms of the governing differential equations and a number of approximate analytic solutions for various volumetric problems were obtained [15][16]. In this thesis we develop a completely new approximation suitable for "volumetric" flaws called the "layer approximation".

1.3 Explanation of Thesis and Format

The work presented in this thesis is part of a larger collaborative project involving (1) my research advisor, James H. Rose, (2) John C. Moulder and (3) Bing Wang. The project, funded by the AFOSR, is aimed at developing methods to detect and characterize corrosion in aircraft lapjoints. Measurements were made by the experimental principal investigator, John Moulder, while the results of the volume integral method were obtained by Bing Wang. A detailed journal article "Impedance of a coil near an imperfectly layered metal structure: perturbation theory" by R. Satveli, J.C. Moulder, B.Wang and J.H. Rose, is in preparation and will be submitted to the Journal of Applied Physics. Portions of the text in this thesis follow this article closely.

The thesis consists of seven chapters. Chapter one introduces the general topic of the thesis. Chapter two states the problem and reviews an analytical solution for the electric field of layered conductors. This solution follows closely the derivation of Dodd and Deeds [4] and the transfer matrix solution of Cheng, Dodd and Deeds [5] for a layered metal, and will be needed for the perturbation theory. Chapter three is devoted to the review of Auld's

reciprocity-based formula. This formula gives the change of impedance due to the presence of a flaw in a layered metal structure. In chapter four, the new method, the layer approximation, is developed. The layer approximation is based on two key ingredients. First, we use Auld's exact reciprocity-based formalism, reviewed in chapter three, for the change in the eddy-current based signal. Second we use the formulas of Cheng, Dodd and Deeds for layered metals, developed in chapter two, to approximate the electric field over the support of the defect. Chapter five presents the results of the layer approximation for a suitably chosen benchmark problem and compares them with experiment and a more exact theoretical treatment. The calculation of impedance change due to localized material loss at the bottom of a metal plate (a flat bottom hole) is the basic problem used to "benchmark" the perturbative method introduced in this thesis. We report experimental measurements [J.C.Moulder] of the impedance of a small, right-cylindrical, air-core coil placed next to a sample consisting of a single layer of 40 mil thick 2024 aluminum. A Hewlett-Packard 4194A impedance analyzer was used to measure the impedance of a series of right-cylindrical flat bottom holes that were of various radii, and at different distances from the center of the coil. Volume element calculations [Bing Wang] were carried out for the same series of flat bottom holes and compared both to the measurements and to the perturbative method. Good agreement is obtained between the calculations and both are in good agreement with the measurements. Chapter six deals with the various additional problems where the perturbation theory was applied. We consider the following canonical problems, all for the impedance of a right-cylindrical air-core coil: (1) a subsurface inclusion in a half-space; (2) metal cladding with a rippled interface; (3) two parallel contiguous metal plates with a volumetric defect at the interface (the lap-joint geometry); and (4) the change in the impedance of two parallel contiguous metal plates due to a fastener, such as a rivet. The final chapter consists of discussion and a summary. Throughout the thesis we denote vectors with a bar over their symbol. All other symbols used in the equations are explained as they appear.

2. ELECTRIC FIELD CALCULATION

2.1 Conductor Geometry

In this chapter, we review the solution for the electric fields in a planar layered conductor due to a right-cylindrical air-core probe. The electric field is calculated since the essential starting point of any perturbation theory is the exact solution of a problem that is "close" in some sense to the problem of interest. The problem of interest in our case is to determine the change in impedance due to a volumetric defect in a layered metal structure. To determine the change of impedance by the perturbation method, one needs the electric fields in the layered metal structure. By applying perturbation theory we reduce our problem to the calculation of electric fields in layered conductor geometry.

The geometry of the sample and the probe are shown schematically in Figure 2.1. The conductivities of the N metal layers are denoted by σ_1 to σ_N . Any layer can be appropriately treated as a vacuum by setting its conductivity equal to zero. The interfaces between the metal layers are located at depths $z=-d_1$ to $z=-d_N$ beneath the vacuum-metal interface at $z=0$. The eddy current probe is located in vacuum above the sample with the bottom of the coil at height l_1 (sometimes referred to as the "lift-off") and the top of the coil at l_2 ; the length of the coil is l_2-l_1 . The inner radius and outer radii of the probe are denoted by r_1 and r_2 . The detailed nature of the wires that constitute the coil is ignored; we assume that the magnitude of the current density is uniform throughout the volume of the coil. In the next section we first outline a procedure for the calculation of the electric field in the layered conductor geometry

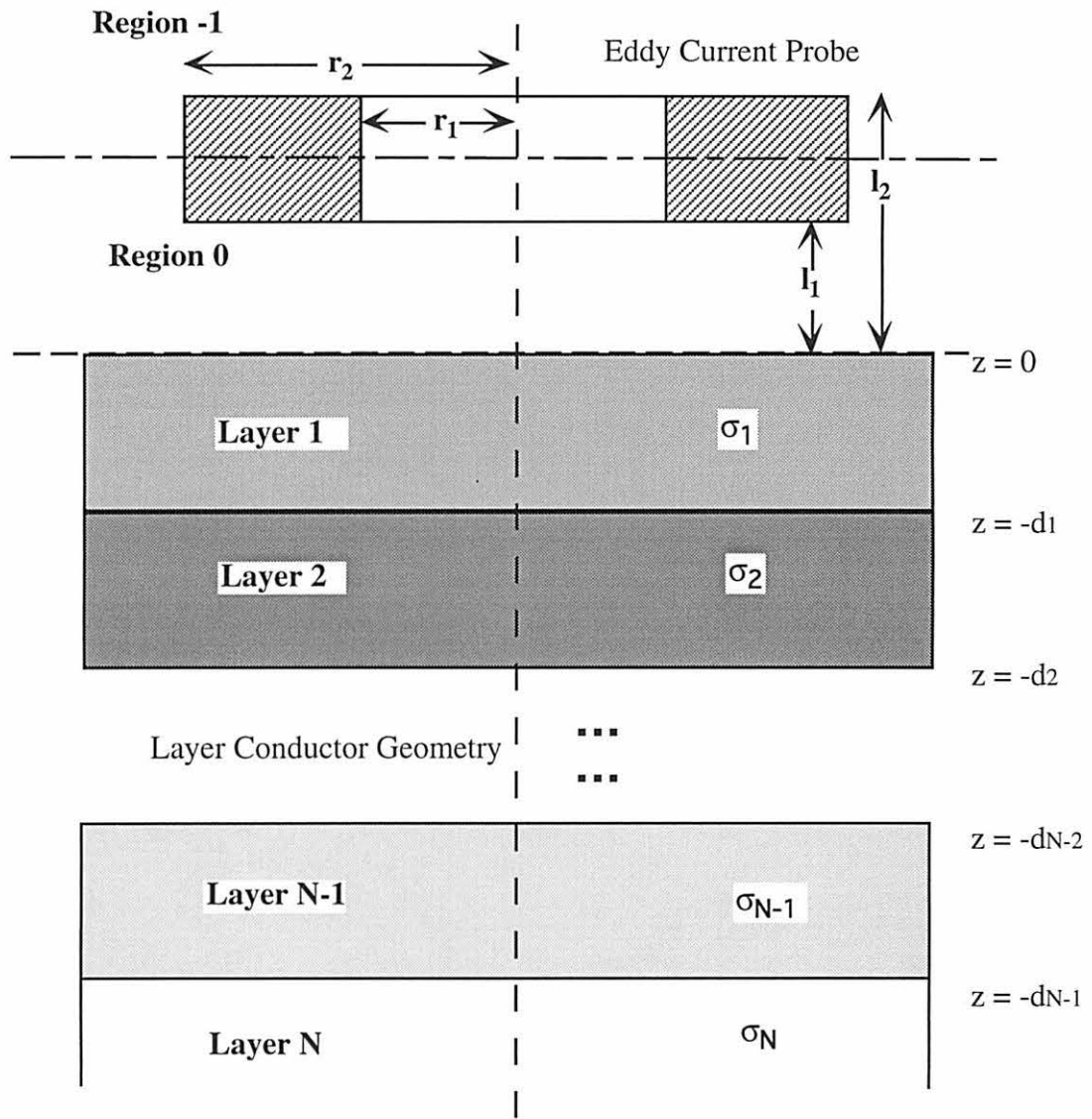


Figure 2.1: Geometry and dimensions of sample and probe

and then implement it in a step by step manner. This procedure is based on the formulas for the vector potential in the layered conductor geometry given by Dodd and Deeds [4] and the transfer matrix solution of Cheng, Dodd and Deeds [5].

2.2 Closed Form Solution of Electric Field

The solution for the electric field at any point in a layered conductor geometry proceeds as follows. We first determine the field generated in the metal by a circular delta-function current filament. This problem can be solved because the conductivity depends only on depth and is thus independent of the coordinates parallel to the surface. Consequently, we can Fourier transform the governing partial differential equation (PDE) for the vector potential in the coordinates parallel to the surface. Due to the circular symmetry of the problem, this becomes a Bessel function expansion. The PDE then decouples into an infinite number of uncoupled ordinary differential equations (ODE's) that are indexed by the transform variables. These ODE's can be solved since they reduce to the scalar wave equation with piece-wise constant complex coefficients. The solution to the PDE is obtained by an inverse transform over the solutions to the ODE's. Finally, the solution for a right-cylindrical coil is obtained by superposing the solutions for the current filaments. This step by step procedure is illustrated below.

The electric field will be computed using the vector potential, \bar{A} , and the Coulomb gauge $\nabla \cdot \bar{A} = 0$. The vector potential is governed by a partial differential equation, which we review below. We start with the relation between the vector potential and the electric field

$$\bar{E} = -\frac{\partial \bar{A}}{\partial t} \tag{2.1}$$

The vector potential, \bar{A} , in a non-magnetic, isotropic, linear and homogeneous medium is governed by the following partial differential equation (PDE):

$$\nabla^2 \bar{A} = \mu_0 \bar{j}_{\text{ext}} + \mu_0 \sigma \frac{\partial \bar{A}}{\partial t} + \mu_0 \varepsilon \frac{\partial^2 \bar{A}}{\partial t^2} \quad (2.2)$$

Here μ_0 denotes the permeability of free space, while ε denotes permittivity. We assume that the external current is sinusoidal and that the coil is cylindrical symmetric. Consequently, the external current can be written as:

$$\bar{j}_{\text{ext}}(r, z) e^{j\omega t} e_{\theta}, \quad (2.3)$$

while the vector potential can be written as:

$$\bar{A}(r, z) e^{j\omega t} e_{\theta}. \quad (2.4)$$

Here, (r, θ, z) are cylindrical coordinates, and e_{θ} denotes the unit vector in the θ -direction.

The external current density for the current filament is

$$I \delta(r - r_0) \delta(z - h) e^{j\omega t} e_{\theta}, \quad (2.5)$$

where r_0 is the radius of the current filament and h is its height above the vacuum-metal interface at $z=0$. We substitute Eqs. (2.3) and (2.4) into Eq. (2.2) and find

$$\frac{\partial^2 A}{\partial r^2} + \frac{1}{r} \frac{\partial A}{\partial r} - \frac{1}{r^2} A + \frac{\partial^2 A}{\partial z^2} = \mu_0 \bar{j}_{\text{ext}} + \mu_0 \sigma j \omega A - \omega^2 \mu_0 \varepsilon A \quad (2.6)$$

We make the quasi static approximation; i.e. we neglect the displacement current, which is represented by the last term on the right-hand-side of Eq. (2.6). This approximation is well satisfied for frequencies below 10 MHz and for conductivities typical of structural metals. The effect is to rule out propagating radio waves. The final form of the PDE for the vector potential is:

$$\frac{\partial^2 A}{\partial r^2} + \frac{1}{r} \frac{\partial A}{\partial r} - \frac{1}{r^2} A + \frac{\partial^2 A}{\partial z^2} = \mu_o j_{ext} + \mu_o \sigma j \omega A \quad (2.7)$$

The boundary conditions for Eq. (2.7) are that A is finite as $r \rightarrow 0$, that A vanishes as $r \rightarrow \infty$ and $z \rightarrow \pm \infty$. A and $\partial A / \partial z$ are continuous at the interfaces between layers where the conductivity changes discontinuously. However $\partial A / \partial z$ jumps at the delta function current sheet.

We consider the solution of Eq. (2.7) for a circular, delta-function filament with its axis parallel to the surface of the half-space. For each layer the general solution of Eq. (2.7) has the form:

$$A(r, z) = \int_0^{\infty} \left(C(\alpha) e^{z\sqrt{\alpha^2 + j\omega\mu\sigma}} + B(\alpha) e^{-z\sqrt{\alpha^2 + j\omega\mu\sigma}} \right) \left(J_1(\alpha r) + D(\alpha) Y_1(\alpha r) \right) d\alpha \quad (2.8)$$

The coefficients B and C are different for each layer. Below, we sketch the transfer matrix method for obtaining these coefficients. The layers are numbered as shown in Figure 2.1. The region above the current filament is denoted by "-1". The region between the filament and the plate by "0". Each of the layers are numbered 1 through N. The last layer, N, is infinite in depth and extends to $z \rightarrow -\infty$. The fact that the vector potential is finite as $r \rightarrow 0$, implies that D is zero for all layers since $Y_1(\alpha r)$ diverges as $r \rightarrow 0$. Similarly, the fact that the vector potential vanishes for large z implies that $C(\alpha)$ is zero for the region above the filament

(region -1). Finally, the fact that the vector potential is zero for large negative z implies that $B(\alpha)$ is zero in region N. The vector potential equations in various regions as obtained from Eq (2.8) are as given below:

$$A^{-1}(r, z) = \int_0^{\infty} B_{-1}(\alpha) e^{-\alpha z} J_1(\alpha r) d\alpha \quad (2.9a)$$

$$A^0(r, z) = \int_0^{\infty} [C_0(\alpha) e^{\alpha z} + B_0(\alpha) e^{-\alpha z}] J_1(\alpha r) d\alpha - \mu_0 I \delta(r - r_0) \quad (2.9b)$$

$$A^1(r, z) = \int_0^{\infty} [C_1(\alpha) e^{\alpha z} + B_1(\alpha) e^{-\alpha z}] J_1(\alpha r) d\alpha \quad (2.9c)$$

$$A^2(r, z) = \int_0^{\infty} [C_2(\alpha) e^{\alpha z} + B_2(\alpha) e^{-\alpha z}] J_1(\alpha r) d\alpha \quad (2.9d)$$

...

...

...

$$A^{N-2}(r, z) = \int_0^{\infty} [C_{N-2}(\alpha) e^{\alpha z} + B_{N-2}(\alpha) e^{-\alpha z}] J_1(\alpha r) d\alpha \quad (2.9e)$$

$$A^{N-1}(r, z) = \int_0^{\infty} [C_{N-1}(\alpha) e^{\alpha z} + B_{N-1}(\alpha) e^{-\alpha z}] J_1(\alpha r) d\alpha \quad (2.9f)$$

$$A^N(r, z) = \int_0^{\infty} [C_N(\alpha) e^{\alpha z}] J_1(\alpha r) d\alpha \quad (2.9g)$$

Here B_{-1} to B_{N-1} and C_0 to C_N are the coefficients corresponding to different layers and α_i depends on the layer conductivity, σ_i , as per the relation $\alpha_i = \sqrt{\alpha^2 + j\omega\mu_0\sigma_i}$.

Due to the continuous nature of the vector potential, we have a set of boundary conditions:

At $z=L$:

($\partial A/\partial z$ jumps due to the delta function current sheet.)

$$A^{-1}(r, l) = A^0(r, l) \quad (2.10a1)$$

$$\frac{\partial}{\partial z} A^{-1}(r, z)|_{z=l} = \frac{\partial}{\partial z} A^0(r, z)|_{z=l} - \mu_0 I \delta(r - r_0) \quad (2.10a2)$$

At $z=0$:

$$A^0(r, 0) = A^1(r, 0) \quad (2.10b1)$$

$$\frac{\partial}{\partial z} A^0(r, z)|_{z=0} = \frac{\partial}{\partial z} A^1(r, z)|_{z=0} \quad (2.10b2)$$

At $z=d_1$:

$$A^1(r, -d_1) = A^2(r, -d_1) \quad (2.10c1)$$

$$\frac{\partial}{\partial z} A^1(r, z)|_{z=-d_1} = \frac{\partial}{\partial z} A^2(r, z)|_{z=-d_1} \quad (2.10c2)$$

...

...

...

At $z=d_{N-2}$:

$$A^{N-2}(r, -d_{N-2}) = A^{N-1}(r, -d_{N-2}) \quad (2.10d1)$$

$$\frac{\partial}{\partial z} A^{N-2}(r, z)|_{z=-d_{N-2}} = \frac{\partial}{\partial z} A^{N-1}(r, z)|_{z=-d_{N-2}} \quad (2.10d2)$$

At $z=d_{N-1}$:

$$A^{N-1}(r, -d_{N-1}) = A^N(r, -d_{N-1}) \quad (2.10e1)$$

$$\frac{\partial}{\partial z} A^{N-1}(r, z)|_{z=-d_{N-1}} = \frac{\partial}{\partial z} A^N(r, z)|_{z=-d_{N-1}} \quad (2.10e2)$$

Substituting the vector potentials in the boundary condition equations (i.e. Eqs. (2.9) in Eqs. (2.10)), we have a set of simultaneous equations which are solved for the constants B_{-1} to B_{N-1} , and C_0 to C_N :

At $z=L$:

$$B_{-1}e^{-\alpha l} = C_0e^{\alpha l} + B_0e^{-\alpha l} \quad (2.11a1)$$

$$-B_{-1}e^{-\alpha l} = C_0e^{\alpha l} - B_0e^{-\alpha l} - \mu_0 i_0 r_0 J_1(\alpha r_0) \quad (2.11a2)$$

At $z=0$:

$$C_0 + B_0 = C_1 + B_1 \quad (2.11b1)$$

$$C_0 - B_0 = \frac{\alpha_1}{\alpha} C_1 - \frac{\alpha_1}{\alpha} B_1 \quad (2.11b2)$$

At $z=d_1$:

$$C_1 e^{-\alpha_1 d_1} + B_1 e^{\alpha_1 d_1} = C_2 e^{-\alpha_2 d_1} + B_2 e^{\alpha_2 d_1} \quad (2.11c1)$$

$$C_1 e^{-\alpha_1 d_1} - B_1 e^{\alpha_1 d_1} = \frac{\alpha_2}{\alpha_1} C_2 e^{-\alpha_2 d_1} - \frac{\alpha_2}{\alpha_1} B_2 e^{\alpha_2 d_1} \quad (2.11c2)$$

...

...

...

At $z=d_{N-2}$:

$$C_{N-2} e^{-\alpha_{N-2} d_{N-2}} + B_{N-2} e^{\alpha_{N-2} d_{N-2}} = C_{N-1} e^{-\alpha_{N-1} d_{N-2}} + B_{N-1} e^{\alpha_{N-1} d_{N-2}} \quad (2.11d1)$$

$$C_{N-2} e^{-\alpha_{N-2} d_{N-2}} - B_{N-2} e^{\alpha_{N-2} d_{N-2}} = \frac{\alpha_{N-1}}{\alpha_{N-2}} C_{N-1} e^{-\alpha_{N-1} d_{N-2}} - \frac{\alpha_{N-1}}{\alpha_{N-2}} B_{N-1} e^{\alpha_{N-1} d_{N-2}} \quad (2.11d2)$$

At $z=d_{N-1}$:

$$C_{N-1} e^{-\alpha_{N-1} d_{N-1}} + B_{N-1} e^{\alpha_{N-1} d_{N-1}} = C_N e^{-\alpha_N d_{N-1}} \quad (2.11e1)$$

$$C_{N-1}e^{-\alpha_{N-1}d_{N-1}} - B_{N-1}e^{\alpha_{N-1}d_{N-1}} = \frac{\alpha_N}{\alpha_{N-1}}C_N e^{-\alpha_N d_{N-1}} \quad (2.11e2)$$

C_0 for single delta function coil is determined from Eqs. (2.11a1) and (2.11a2) as:

$$C_0 = \frac{\mu i_0 r_0 J_1(\alpha r_0)}{e^{\alpha l}} \quad (2.12)$$

The vector potential for a coil of finite cross-section can be obtained by superposing the filament:

$$A(r,z)(\text{total}) = \int_{\text{Coil Cross Section}} A(r,z,r_0,l)d(\text{area}) \quad (2.13)$$

$$\text{i.e. } A(r,z)(\text{total}) = \int_{r_1}^{r_2} \int_{l_1}^{l_2} A(r,z,r_0,l)dr_0 dl \quad (2.14)$$

Upon integrating C_0 over the cross sectional area of the coil, we find:

$$C_0 = -\frac{\mu IP(r_2,r_1)}{\alpha^3}(e^{-\alpha l_2} - e^{-\alpha l_1}) \quad (2.15)$$

Here

$$\int_{r_1}^{r_2} r_0 J_1(\alpha r_0) dr_0 = \frac{1}{\alpha^2} \int_{\alpha r_1}^{\alpha r_2} x J_1(x) dx = \frac{1}{\alpha^2} P(r_2,r_1) \quad (2.16)$$

and

$$\int_{l_1}^{l_2} e^{-\alpha l} dl = \frac{e^{-\alpha l_2} - e^{-\alpha l_1}}{-\alpha}. \quad (2.17)$$

Also the current density is related to the total current in the coil as:

$$i_o = \frac{nI}{(l_2 - l_1)(r_2 - r_1)} \quad (2.18)$$

where n represents the number of turns in the eddy current probe and the denominator specifies the cross section area of the coil. Therefore, for a coil of finite cross section, the value of C_0 as given in Eq. (2.15) is used instead of the one obtained for single delta function coil as in Eq. (2.12).

2.3 Constant Determination by Recursive Technique

Once C_0 is known, the rest of the constants are determined by recursion. Eqs. (2.11b1) to (2.11e2) are represented in matrix notation as:

$$\begin{pmatrix} C_0 \\ B_0 \end{pmatrix} = \begin{pmatrix} \frac{\alpha_1 + \alpha}{2\alpha} & \frac{\alpha - \alpha_1}{2\alpha} \\ \frac{\alpha - \alpha_1}{2\alpha} & \frac{\alpha_1 + \alpha}{2\alpha} \end{pmatrix} \begin{pmatrix} C_1 \\ B_1 \end{pmatrix} \quad (2.19a)$$

$$\begin{pmatrix} C_1 \\ B_1 \end{pmatrix} = \begin{pmatrix} \frac{\alpha_1 + \alpha_2}{2\alpha_1} e^{-d_1(\alpha_2 - \alpha_1)} & \frac{\alpha_1 - \alpha_2}{2\alpha_1} e^{d_1(\alpha_2 + \alpha_1)} \\ \frac{\alpha_1 - \alpha_2}{2\alpha_1} e^{-d_1(\alpha_2 + \alpha_1)} & \frac{\alpha_1 + \alpha_2}{2\alpha_1} e^{-d_1(\alpha_1 - \alpha_2)} \end{pmatrix} \begin{pmatrix} C_2 \\ B_2 \end{pmatrix} \quad (2.19b)$$

...

...

...

$$\begin{pmatrix} C_{N-2} \\ B_{N-2} \end{pmatrix} = \begin{pmatrix} \frac{\alpha_{N-2} + \alpha_{N-1}}{2\alpha_{N-2}} e^{-d_{N-2}(\alpha_{N-1} - \alpha_{N-2})} & \frac{\alpha_{N-2} - \alpha_{N-1}}{2\alpha_{N-2}} e^{d_{N-2}(\alpha_{N-1} + \alpha_{N-2})} \\ \frac{\alpha_{N-2} - \alpha_{N-1}}{2\alpha_{N-2}} e^{-d_{N-2}(\alpha_{N-1} + \alpha_{N-2})} & \frac{\alpha_{N-2} + \alpha_{N-1}}{2\alpha_{N-2}} e^{-d_{N-2}(\alpha_{N-1} - \alpha_{N-1})} \end{pmatrix} \begin{pmatrix} C_{N-1} \\ B_{N-1} \end{pmatrix} \quad (2.19c)$$

$$\begin{pmatrix} C_{N-1} \\ B_{N-1} \end{pmatrix} = \begin{pmatrix} \frac{\alpha_{N-1} + \alpha_N}{2\alpha_{N-1}} e^{-d_{N-1}(\alpha_N - \alpha_{N-1})} \\ \frac{\alpha_{N-1} - \alpha_N}{2\alpha_{N-1}} e^{-d_{N-1}(\alpha_N + \alpha_{N-1})} \end{pmatrix} \begin{pmatrix} C_N \\ 0 \end{pmatrix} \quad (2.19d)$$

The Eqs. (2.19a) to (2.19d) together yield:

$$\begin{pmatrix} C_o \\ B_o \end{pmatrix} = \begin{pmatrix} \frac{\alpha_1 + \alpha}{2\alpha} & \frac{\alpha - \alpha_1}{2\alpha} \\ \frac{\alpha - \alpha_1}{2\alpha} & \frac{\alpha_1 + \alpha}{2\alpha} \end{pmatrix} \begin{pmatrix} \frac{\alpha_1 + \alpha_2}{2\alpha_1} e^{-d_1(\alpha_2 - \alpha_1)} & \frac{\alpha_1 - \alpha_2}{2\alpha_1} e^{d_1(\alpha_2 + \alpha_1)} \\ \frac{\alpha_1 - \alpha_2}{2\alpha_1} e^{-d_1(\alpha_2 + \alpha_1)} & \frac{\alpha_1 + \alpha_2}{2\alpha_1} e^{-d_1(\alpha_1 - \alpha_2)} \end{pmatrix} \cdots \begin{pmatrix} \frac{\alpha_{N-1} + \alpha_N}{2\alpha_{N-1}} e^{-d_{N-1}(\alpha_N - \alpha_{N-1})} \\ \frac{\alpha_{N-1} - \alpha_N}{2\alpha_{N-1}} e^{-d_{N-1}(\alpha_N + \alpha_{N-1})} \end{pmatrix} \begin{pmatrix} C_N \\ 0 \end{pmatrix} \quad (2.20)$$

C_N and B_o can be calculated from Eq. (2.20) since C_o is known. Substituting C_N in Eq. (2.19d) we find C_{N-1} and B_{N-1} . Similarly substituting C_{N-1} and B_{N-1} in Eq. (2.19c) the values of C_{N-2} and B_{N-2} are determined. We continue the recursive process till all the constants are found. The vector potential in various regions of the conductor geometry can be found by substituting these values of coefficients in the corresponding vector potential formulae given by Eqs. (2.9). The electric field is calculated from the vector potential, Eq. (2.1),

$$\vec{E} = -j\omega\vec{A}. \quad (2.21)$$

The closed form solutions for the electric field in the region above the current filament (denoted by -1), in the region between the region and the plate (denoted by 0) and in some particular layer "k" are given by:

$$E^{-1}(r, z, \omega) = -j\omega \int_0^{\infty} B_{-1}(\alpha) e^{-\alpha z} J_1(\alpha r) d\alpha \quad (2.22a)$$

$$E^0(r, z, \omega) = -j\omega \int_0^{\infty} [C_0(\alpha) e^{\alpha z} + B_0(\alpha) e^{-\alpha z}] J_1(\alpha r) d\alpha - \mu i_0 \delta(r - r_0) \quad (2.22b)$$

$$E^k(r, z, \omega) = -j\omega \int_0^{\infty} [C_k(\alpha) e^{\alpha z} + B_k(\alpha) e^{-\alpha z}] J_1(\alpha r) d\alpha \quad (2.22c)$$

2.4 Program Listings

The software provides a user interface for the input parameters of the conductor geometry and the eddy current probe, and calculates electric field in any specified region based on the values of r and z (i.e. the radius and the depth) in reference to the axis of the conductor geometry shown in Figure 2.1. The listings are in C.

3. RECIPROCALITY-BASED FORMULA FOR CHANGE IN IMPEDANCE

In this chapter, we review Auld's exact reciprocity-based formula that determines the change in the impedance of an air-core probe for the generic problem shown schematically in Figure 3.1b. Auld's formula is the basis for the layer approximation that is developed in chapter five. We imagine measuring the frequency-dependent impedance, Z_f , of a small right-cylindrical air-core coil placed next to a layered metal structure with N layers and a localized defect as shown in Figure. 3.1b. Next, we imagine measuring the impedance, Z_0 , of a defect-free reference sample as shown in Figure. 3.1a. The problem addressed in this chapter is to determine the change in the impedance, $\delta Z = Z_f - Z_0$. For concreteness, we suppose that a constant ac current is applied to the coil and that the resulting voltage drop is measured. Finally, the impedance is inferred from the flaw induced voltage. In order to determine the change in impedance, we review Auld's exact reciprocity-based formalism for the change in the eddy-current signal. Auld's formalism predicts the change in the impedance if the exact electric field in the region of the defect is known.

3.1 Reciprocity Formula

In this section, we review the derivation of Auld's reciprocity formula from the basic electromagnetic equations. The derivation given in Ref.11, an unpublished manuscript by Auld and Moulder, is followed closely. The input power, P_{IN} , of the eddy current probe can be given as:

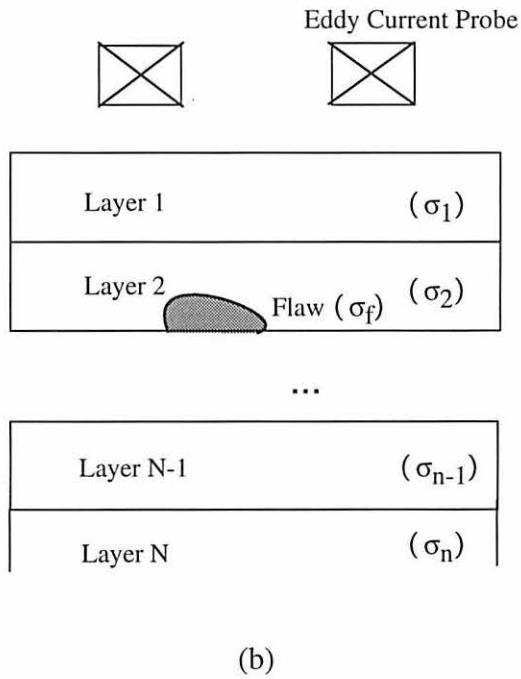
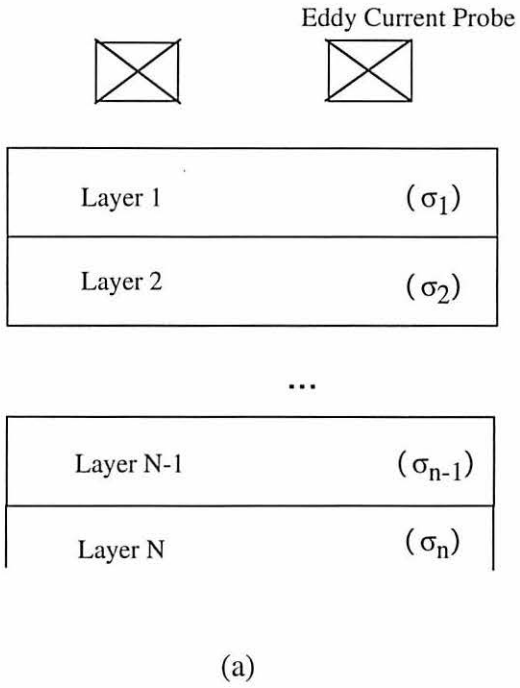


Figure 3.1: (a) Reference case, without any flaw
 (b) Actual layered geometry, with a flaw

$$P_{IN} = \frac{VI^*}{2} = \frac{ZI^*}{2} \quad (3.1)$$

Applying Poynting theorem, the input power in terms of electromagnetic field distributions \bar{E} and \bar{H} , corresponding to voltage (V) and current (I) is:

$$P_{IN} = \frac{1}{2} \int_{S_c} \bar{E} \times \bar{H} \cdot \hat{n} ds \quad (3.2)$$

where S_c is the area of the co-axial line section at the terminal plane as shown in Figure 3.2. Equating Eq. (3.1) and Eq. (3.2) and dropping conjugate sign (zero phase of input current at the terminal plane):

$$Z = \frac{2P_{IN}}{I^2} = \frac{1}{I^2} \int_{S_c} \bar{E} \times \bar{H} \cdot \hat{n} ds \quad (3.3)$$

The impedance Z_0 , for the layer conductor geometry of Figure 3.1a, i.e. in absence of any flaw can be obtained from Eq. (3.3) as:

$$Z_0 = \frac{1}{I^2} \int_{S_c} \bar{E}_0 \times \bar{H}_0 \cdot \hat{n} ds \quad (3.4)$$

where \bar{E}_0 and \bar{H}_0 are probe fields in the absence of flaw.

Similarly, the impedance Z_f in the presence of flaw as shown in Figure. 3.1b is:

$$Z_f = \frac{1}{I^2} \int_{S_c} \bar{E}_f \times \bar{H}_f \cdot \hat{n} ds \quad (3.5)$$

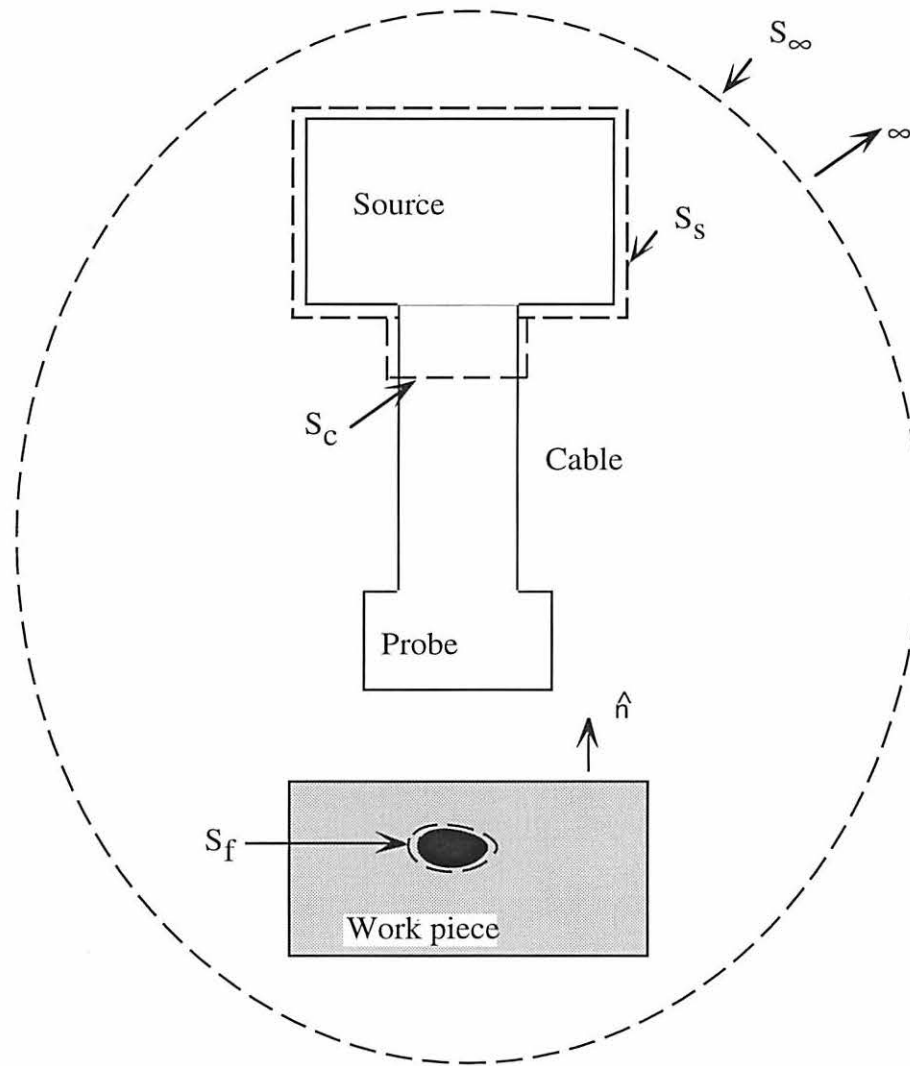


Figure 3.2: Schematic diagram of eddy-current apparatus showing various surfaces

where $\overline{\mathbf{E}}_r$ and $\overline{\mathbf{H}}_r$ are the probe fields in the presence of flaw.

The change in impedance due to the flaw is the difference in the value of Z in the presence (Z_f) and the absence (Z_o) of the flaw and is represented by δZ .

$$\delta Z = Z_f - Z_o = -\frac{1}{I^2} \int_{S_c} (\overline{\mathbf{E}}_o \times \overline{\mathbf{H}}_o - \overline{\mathbf{E}}_r \times \overline{\mathbf{H}}_r) \cdot \hat{n} ds \quad (3.6)$$

Because $\overline{\mathbf{H}}$ at S_c is proportional to the input current, which is assumed to be a constant I , it follows that $\overline{\mathbf{H}}_o = \overline{\mathbf{H}}_r$ on S_c . Therefore Eq. (3.6) can be written as:

$$\delta Z = Z_f - Z_o = -\frac{1}{I^2} \int_{S_c} (\overline{\mathbf{E}}_o \times \overline{\mathbf{H}}_r - \overline{\mathbf{E}}_r \times \overline{\mathbf{H}}_o) \cdot \hat{n} ds \quad (3.7)$$

The expression for δZ can be converted to a field integral over the flaw by invoking the Lorenz reciprocity relationship [12]

$$(\overline{\mathbf{E}}_r \times \overline{\mathbf{H}}_o - \overline{\mathbf{E}}_o \times \overline{\mathbf{H}}_r) = 0 \quad (3.8)$$

between arbitrary solutions to Maxwell's equation in a source free region with fixed material properties. In particular Eq. (3.8) applies to the fields defined in Eq. (3.4) and Eq. (3.5) at all points exterior to the source and the flaw. Also the integral around the source reduces to an integral over the coaxial cross section S_c [11]. Thereby the surface integral in Eq. (3.7) gives an expression for δZ in terms of an integral over the flaw S_f .

$$\delta Z = Z_f - Z_o = -\frac{1}{I^2} \int_{S_f} (\overline{\mathbf{E}}_o \times \overline{\mathbf{H}}_r - \overline{\mathbf{E}}_r \times \overline{\mathbf{H}}_o) \cdot \hat{n} ds \quad (3.9)$$

As we deal only with finite volume flaws in this thesis, it is convenient to express δZ as a volume integral rather than a surface integral. This is accomplished by first using the divergence theorem to write Eq. (3.9) as:

$$\delta Z = -\frac{1}{I^2} \int_{V_F} \nabla \cdot (\bar{\mathbf{E}}_o \times \bar{\mathbf{H}}_r - \bar{\mathbf{E}}_r \times \bar{\mathbf{H}}_o) dV \quad (3.10)$$

where V_F is the volume enclosed by S_F . Using the identity

$$\nabla \cdot (\bar{\mathbf{A}} \times \bar{\mathbf{B}}) = \bar{\mathbf{B}} \cdot \nabla \times \bar{\mathbf{A}} - \bar{\mathbf{A}} \cdot \nabla \times \bar{\mathbf{B}} \quad (3.11)$$

and Maxwell's equations, Eq. (3.10) can be converted to volume integral format:

$$\delta Z = -\frac{i\omega}{I^2} \int_{V_F} (\bar{\mathbf{H}}_o \cdot [\delta\boldsymbol{\mu} \cdot \bar{\mathbf{H}}_r] - \bar{\mathbf{E}}_o \cdot [\delta\boldsymbol{\varepsilon} \cdot \bar{\mathbf{E}}_r]) dV \quad (3.12)$$

Due to the dominance of conduction current over the displacement current we make the quasi-static approximation:

$$\boldsymbol{\varepsilon} + \frac{\boldsymbol{\sigma}}{i\omega} \approx \frac{\boldsymbol{\sigma}}{i\omega} \quad (3.13)$$

The volume integral form then reduces to Auld's formula [10]:

$$\delta Z(\omega) = -\frac{1}{I^2} \int d^3\bar{y} \delta\sigma(\bar{y}) \bar{\mathbf{E}}_o(\omega, \bar{y}) \cdot \bar{\mathbf{E}}_r(\omega, \bar{y}) \quad (3.14)$$

Here, $\delta\sigma = \sigma - \sigma_0$, denotes the difference in conductivity between the flawed sample and the reference sample (i.e. without flaw), while I denotes the current in the coil, ω denotes the angular frequency and \bar{y} denotes the spatial coordinate. \bar{E}_f denotes the electric field in the flawed part, while \bar{E}_0 denotes the electric field in the reference part. Eq. (3.14) is particularly useful for perturbation theory because it only requires that \bar{E}_0 and \bar{E}_f be estimated in the region (support) of the defect since $\delta\sigma$ is zero elsewhere. It is not necessary to estimate the electric fields in the region of the coil.

The main disadvantage of Auld's formula is that it requires the determination of the exact electric field in the region of the flaw. The electric field in the presence of flaw depends on the shape and size of the flaw and does not have an exact analytical solution. To overcome this disadvantage, we apply perturbation theory and develop a new technique called the layer approximation in the next chapter.

4. PERTURBATION THEORY

The layer approximation, developed in this chapter, determines the change in the impedance of an air-core probe due to the presence of a flaw in a layered metal structure by employing a perturbation approach. The generic problem is shown schematically in Figure 4.1b. The metal structure without flaw is shown in Figure 4.1a.

4.1 An Introduction

Auld's formula (Eq. (3.14)), reviewed in chapter three, gives the exact solution for the change in impedance, $\delta Z = Z_f - Z_o$ where Z_f is the impedance in the presence of the flaw and Z_o is the impedance in the absence of the flaw. As was seen in chapter three, Auld's formula requires the knowledge of exact electric field in presence of the flaw (\bar{E}_f), a quantity that is rarely available. As the electric field in the presence of the flaw does not have a closed formula, there is need for approximations. Approximate solutions for δZ can be obtained by substituting in guesses for \bar{E}_f . We resort to approximations for \bar{E}_f by applying perturbation theory. Perturbation techniques are efficient and allow acceptable precision if an unsolvable problem is "close" to a problem whose solution is known. One approximation would be to replace the field in the presence of the flaw, \bar{E}_f , with the incident field, \bar{E}_o . The result is:

$$\delta Z_b(\omega) = -\frac{1}{I^2} \int d^3y \delta\sigma(y) \bar{E}_o(\omega, \bar{y}) \cdot \bar{E}_o(\omega, \bar{y}) \quad (4.1)$$

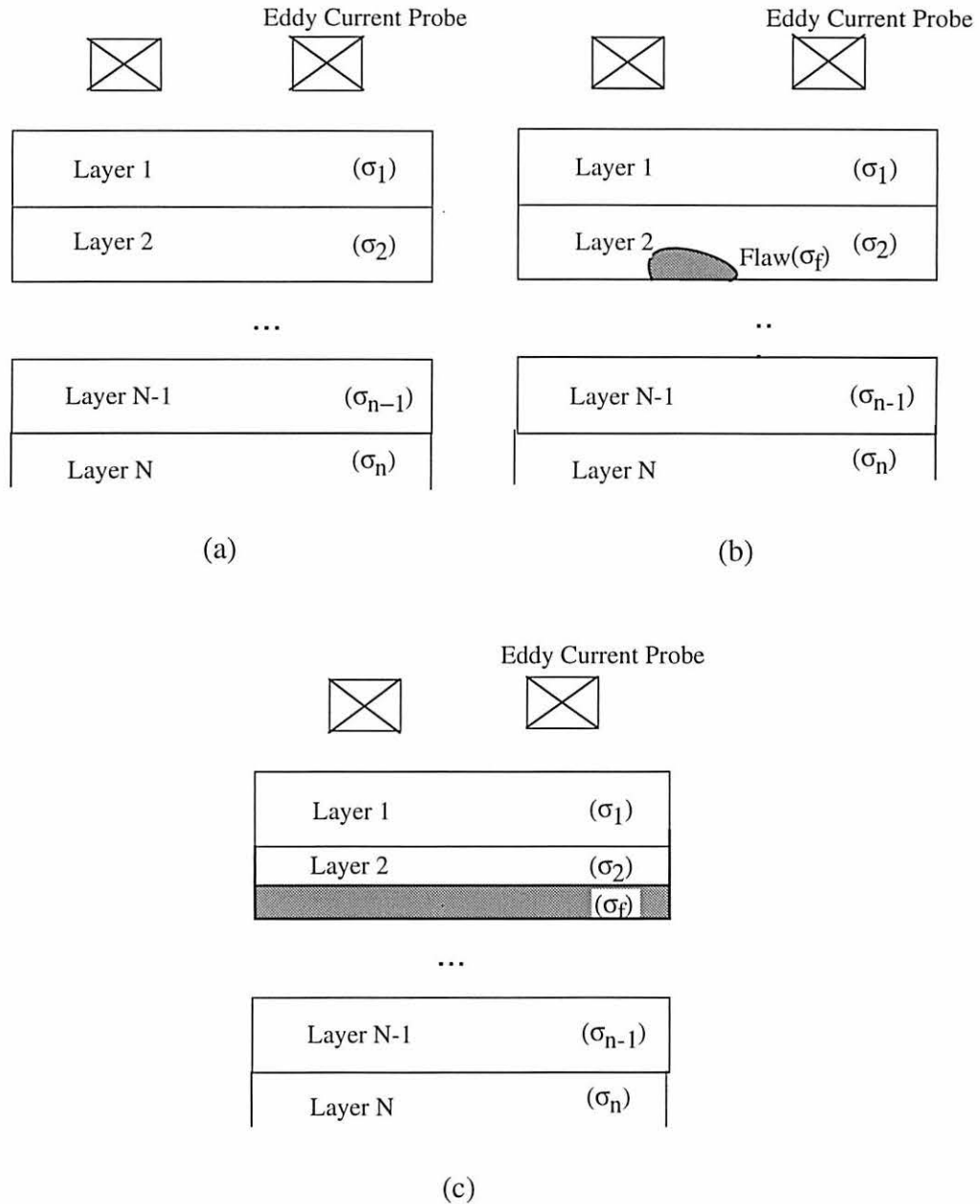


Figure 4.1: (a) Reference case, without any flaw
 (b) Actual layered geometry, with a flaw
 (c) Layer approximation, with additional layer

Eq. (4.1) is called the Born approximation, and is reasonable only if the relative change in conductivity is small. To partially overcome this limitation, we propose a versatile approximation called the layer approximation in the next section. It advances the generic problem of flaw characterization in layered conductor geometry. The layer approximation assumes that the defect is not crack-like, that it is localized and that either (1) the relative change in conductivity introduced by the defect is very small or (2) that the sample is very nearly one-dimensional (i.e. layered) in the region where the coil's electric field is significant.

4.2 The Layer Approximation

The layer approximation is based on two key ingredients (covered in previous chapters). First, we use Auld's exact reciprocity-based formalism [10] for the change in the eddy-current signal. Second we use the formulas of Cheng, Dodd and Deeds [5] for layered metals to approximate the electric field over the support of the defect. By judiciously combining these two ingredients we obtain the desired approximation.

The layer approximation is derived as follows. Let us suppose that the defect is localized (i.e. has finite support) and that either (1) the change in conductivity is sufficiently small

$$\frac{\delta\sigma}{\sigma_0} \ll 1,$$

or (2) that the defect is itself nearly layered in the region of the coil. We wish to calculate the change in the impedance that is induced by a defect in layered sample. For the purposes of the derivation, we imagine an additional hypothetical layered sample. This additional sample is

constructed to be the same as the original sample except that it contains a layer with the conductivity of the defect. The additional layer is chosen to overlap the support of the defect but to otherwise be as thin as possible. We compute the electric field, \bar{E}_L , that would occur for this hypothetical sample. The layer approximation for the impedance change, δZ_L , is then obtained by substituting \bar{E}_L in Eq. (3.14).

$$\delta Z_L(\omega) = -\frac{1}{I^2} \int d^3y \delta\sigma(y) \bar{E}_o(\omega, \bar{y}) \cdot \bar{E}_L(\omega, \bar{y}) \quad (4.2)$$

In order to make the layer approximation as clear as possible, we consider the flawed sample shown in Fig. 4.1b as an example. The electric field, \bar{E}_L , is calculated for a plate, whose thickness has been reduced by the height of the flaw as shown in Fig. 4.1c. An additional layer with the conductivity of the flaw is introduced instead. The key point is that \bar{E}_L is calculated for a sample that has the same conductivity as the defect over the support of the defect.

In the succeeding chapters we will compare the layer approximation with the experimental results for a benchmark problem that represents a fairly extreme test of the approximation. In addition, we compare the layer approximation to more exact theoretical calculations for the benchmark problem. Further we will compare the layer approximation to the Born approximation. These comparisons, as will be seen, show that the layer approximation is reasonably accurate and provides a good tool for calculating changes of impedance due to defects in a layered metal structure. Finally, to show the versatility of the layer approximation, we apply it to various problems of interest to industry.

5. THE BENCHMARK PROBLEM

In this chapter the question of "How robust is the new perturbation approximation ?" is answered. In order to do so, we apply the layer approximation to a "benchmark problem". We first present the problem. This problem is then solved by the perturbation methods of both the layer approximation and the Born approximation. Next we outline the experimental procedure for obtaining the change in impedance for this benchmark problem and report the measurements. Also a computationally intensive theoretical model called the volume integral method is used to solve the problem. Finally, we also compare the results obtained by these different methods and show that the layer approximation yields accurate results.

5.1 Problem Description

The benchmark problem is to determine the change in the impedance of the a right-cylindrical air-core probe next to a plate that contains a right-cylindrical flat bottom hole on the side opposite to the coil. We use the extreme case of a subsurface void, which has zero conductivity, to test the utility of the layer approximation in a good metal. The test case, a single 1 mm thick plate of 2024 aluminum with a flat bottom hole (i.e. a cylindrical defect) on the side opposite to the coil, is shown in Figure. 5.1. The conductivity of the plate is assumed to be uniform and equal to $1.85e7$ S/m. Our reasoning is that if the layer approximation is accurate for this extreme benchmark case, it is likely to be useful for a wide range of applications. The particular geometry of the test sample was chosen for four reasons. First, it

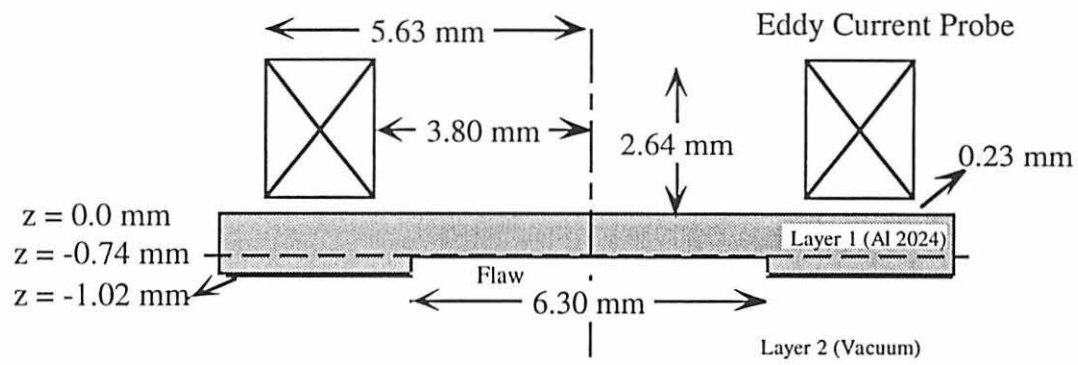


Figure 5.1: The benchmark problem

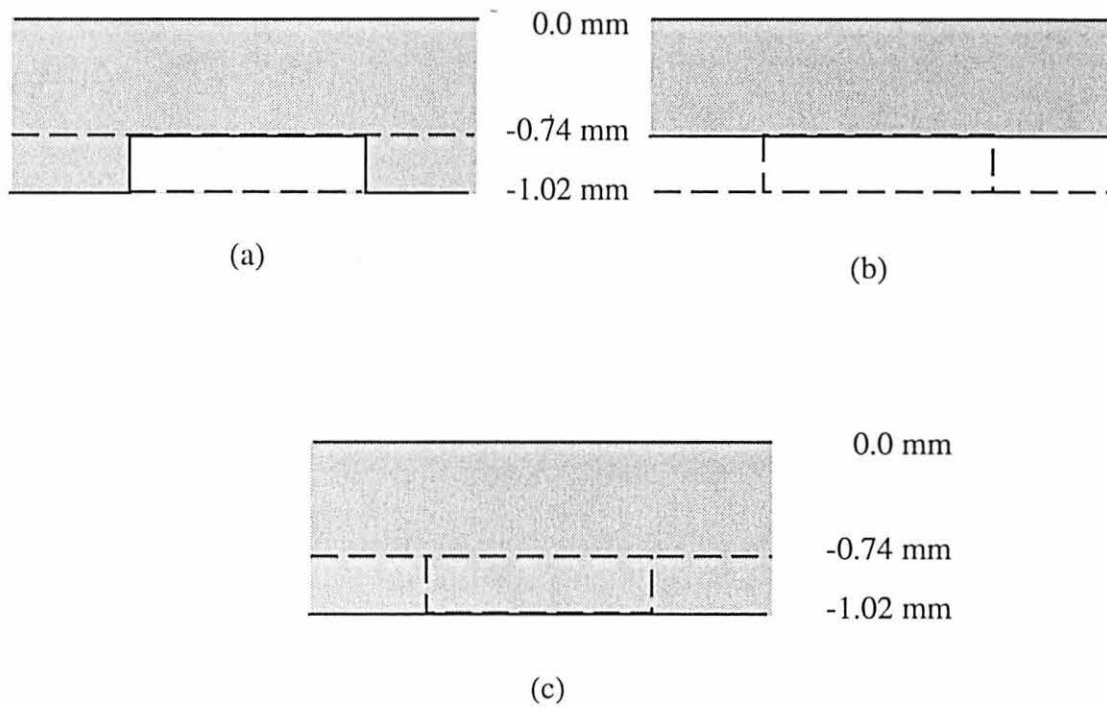


Figure 5.2: (a) Flawed sample for calculation of E_f
 (b) Layer approximation for calculation of E_L
 (c) Reference case for calculation of E_0

is an extreme case. Second, experimental measurements are relatively straightforward. Third, a numerically-exact volume element method has recently been developed to treat defects in this plate geometry [14]. Fourth, the sample simulates pitting corrosion on the hidden side of a plate and is of great industrial utility. The parameters for eddy current probe, conductor geometry and defect dimensions are shown in Table. 5.1.

5.2 Solution by Perturbation Theory

The exact flaw induced change in impedance is given by Eq. (3.14), which is reproduced for readability.

$$\delta Z(\omega) = -\frac{1}{I^2} \int d^3\bar{y} \delta\sigma(\bar{y}) \bar{E}_o(\omega, \bar{y}) \cdot \bar{E}_f(\omega, \bar{y}) \quad (3.14)$$

the integration being over the volume of the cylindrical flaw as in Figure. (5.2a). The reference case would be a sample without any flaw i.e. a single 1.016 mm thick plate of aluminum in vacuum. The electric field \bar{E}_o is calculated for this conductor geometry as shown in Figure. (5.2b). The layer approximation assumes the thickness of the aluminum plate to be reduced by the height of the defect (i.e. by 0.275 mm). This would imply a layer of aluminum which is 0.741 mm thick (1.016 mm - 0.275 mm). The additional layer is introduced in this region with the conductivity of the defect (0.0 S/m in this case). Therefore this layer extends from $z=-0.741$ mm to $z=-1.016$ mm. The conductor geometry for the layer approximation from which \bar{E}_L is calculated is as shown in Figure. 5.2c. The impedance change in the layer approximation is obtained by substituting \bar{E}_L for \bar{E}_f in Eq. (3.14). As seen earlier, substituting \bar{E}_o for \bar{E}_f gives the Born approximation, Eq. (4.1). The change in impedance calculations for the layer and Born approximations are presented in later sections.

Table 5.1: Dimensions of probe, layers geometry and defect

**Eddy Current Probe Description
(A Probe)**

Cross section	Right Cylindrical
Number of turns	504
Inner radius	3.8 mm
Outer radius	5.635 mm
Coil height	2.42 mm
Lift off	0.229 mm

(a)

Conductor Geometry

Number of layers	2
Conductivity of layer 1	1.85×10^7 S/m (Al2024)
Conductivity of layer 2	0.0S/m (Vacuum)
Thickness of layer 1	1.016 mm

(b)

Defect Dimensions

Position of defect	Bottom of layer 1
Defect radius	3.1525 mm
Defect depth	0.275 mm

(c)

5.3 Experimental Procedure for Impedance Measurements

The experimental set-up (Figure 5.3) and the impedance measurements are described in this section. The measurements were made by J.C. Moulder, who has graciously permitted their use in this thesis. We report the impedance change of a precision wound coil of copper wire measured at 20 frequencies equally-spaced between 2.5 kHz and 50 kHz with an HP 4194A impedance analyzer. A 10 cm cable connected the coil to the impedance analyzer. Both the coil and sample were placed in fixtures. The position of the coil was held fixed, while the position of the sample was varied by a precision x-y scanning table, which translated the sample perpendicular to the axis of the coil. Measurements of the coil impedance were made as a function of frequency and of the position with respect to the center of the coil. The impedance change was calculated by taking the impedance when the coil was in the vicinity of the flat bottom hole minus the impedance when the coil was far from the flat bottom hole.

The coil had a right-cylindrical cross-section and consisted of 504 turns of copper wire wound on an insulating nonmagnetic core. The inner radius of the coil was 3.8 mm, the outer diameter was 5.63 mm, while the height of the coil was 2.42 mm. The distance between the bottom of the coil and the top of the plate is termed the "lift-off" and was equal to 0.23 mm. These values are tabulated in Table. 5.1a.

A schematic drawing of the sample is shown in Figure 5.1 while the experimental set-up is shown schematically in Figure 5.3. The sample consists a thin flat plate of 2024 aluminum alloy. The dimensions of the plate were 300 mm x 300m x 1.03 mm. A nominally right-cylindrical hole was drilled on the side of the plate opposite to the coil. The radius of the hole was 6.31 mm and the depth ranged between 0.280 mm at the center to 0.270 mm at the edge. The sample was scanned automatically. Both the impedance analyzer and the scanning table were controlled by a 486 personal computer.

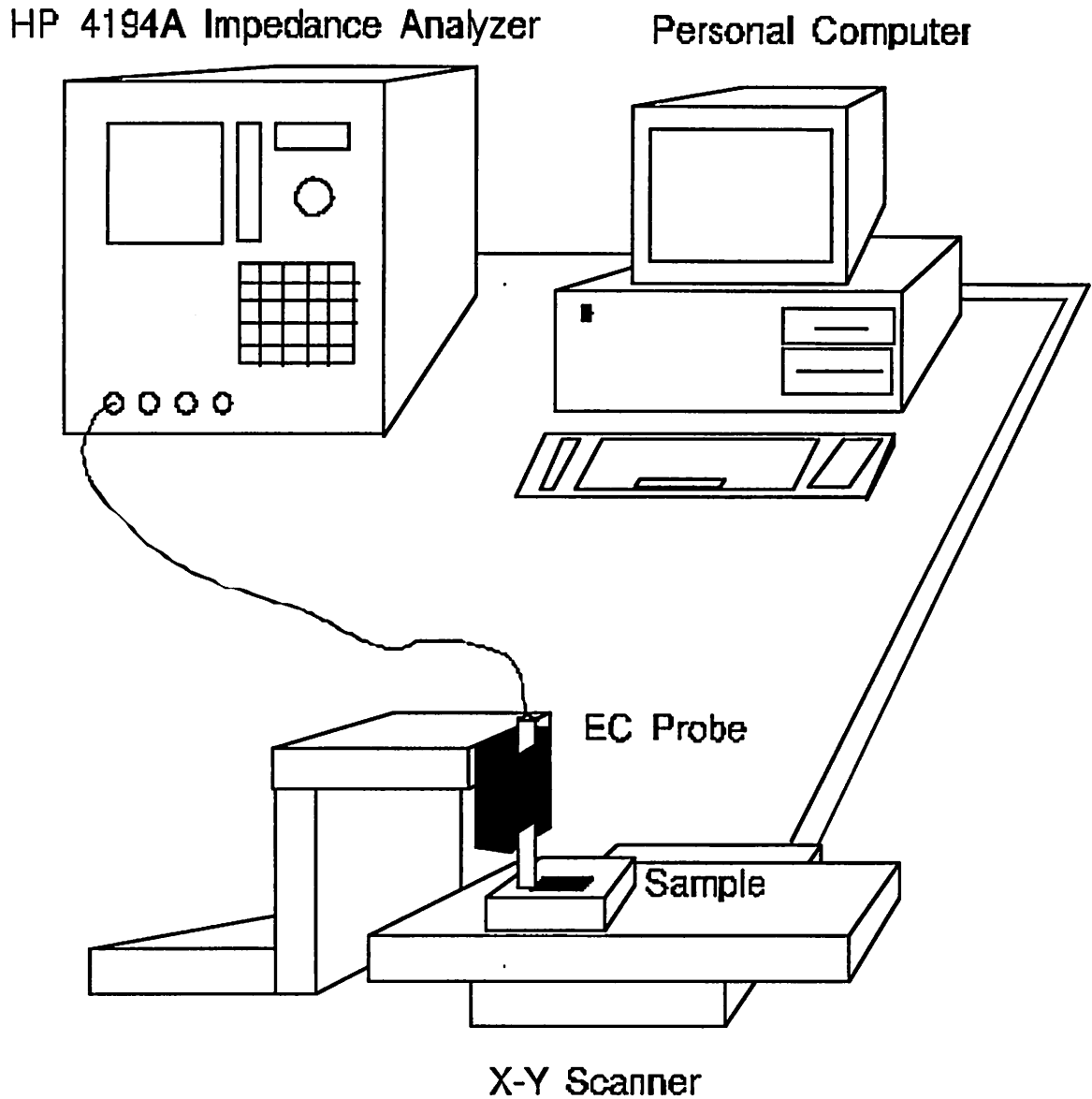


Figure 5.3: Schematic drawing of the experimental set-up. The sample is fixed to a computer controlled x-y scanner. The impedance of the eddy-current (EC) probe is measured by the HP 4194A impedance analyzer.

Figure 5.4 shows the real and imaginary impedance change for a line scan that takes the center of the coil over the center of the defect. The real and imaginary impedance changes were small when the coil was centered far from the defect (e.g., an offset of plus or minus 8 mm). The magnitude of the impedance changes increased when the probe was brought nearer to the center of the defect, reaching a maximum at an offset of plus or minus 4 mm. Finally, the magnitude of the impedance changes decreased and reached a relative minimum with the coil centered with respect to the defect. The signal is cylindrical symmetric, since the probe and defect are also cylindrical symmetric. The current induced in the metal (and the degree to which this current is diverted by the defect) is the key to understanding the shape of the plot. The induced current has the shape of a ring, with the current being strongest directly beneath the wires that constitute the coil (i.e. at -4 and +4 mm). The induced current is zero at the center of the coil (by symmetry). The induced current also decays to zero far away from the coil. Consequently, the signal was small when the flat bottom hole was either centered in the coil or is far from the coil. The signal was the maximum when the defect was immediately beneath the wires.

Consider a scan of the coil over the center of the defect. Figure 5.5a shows the change in the real part of the impedance change plotted as a function of frequency, while Figure. 5.5b shows the change in the imaginary part. The different lines correspond to different off-sets of the coil's center from the flat bottom hole's center. At low frequencies the change in the real part of the impedance was negative for all offset distances. It crossed zero at approximately 5 kHz and reached a maximum at between 15 and 25 kHz and then decreased at higher frequencies. The change in the imaginary part of the impedance was positive at low frequencies, but crossed zero between 12 and 20 kHz; became increasingly negative and then appears to reach a plateau value in the range between 40 and 50 kHz.

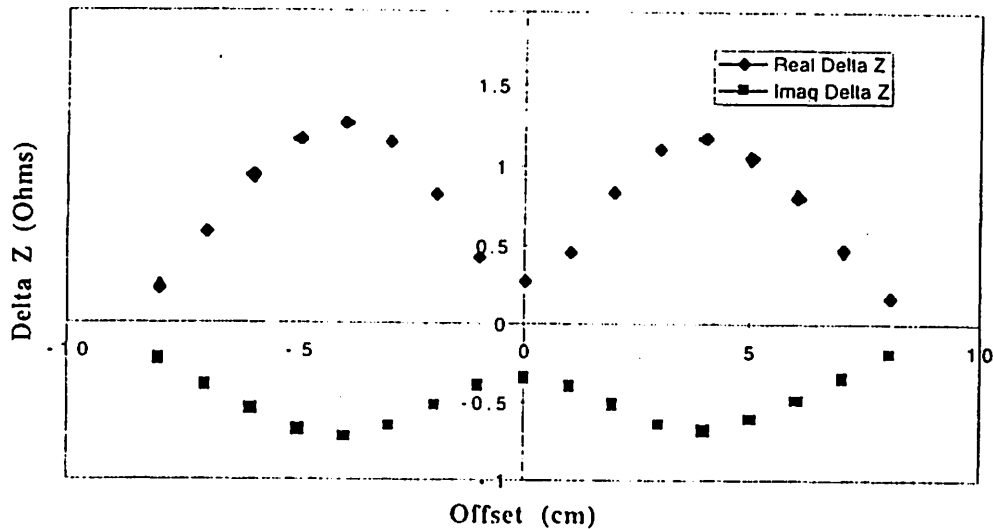
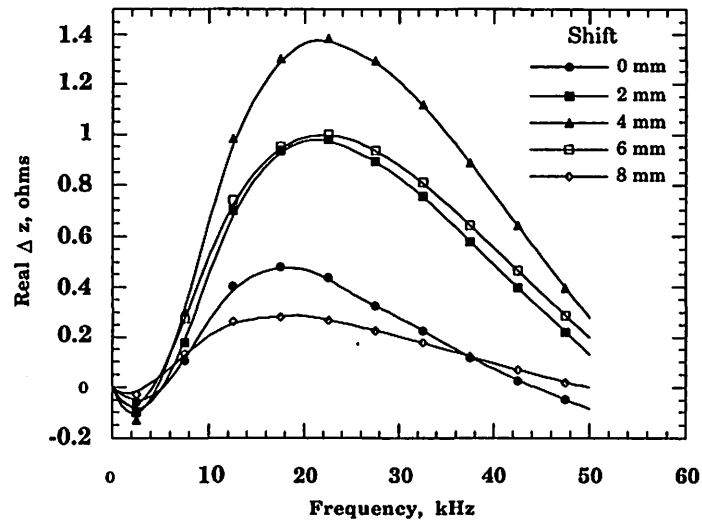


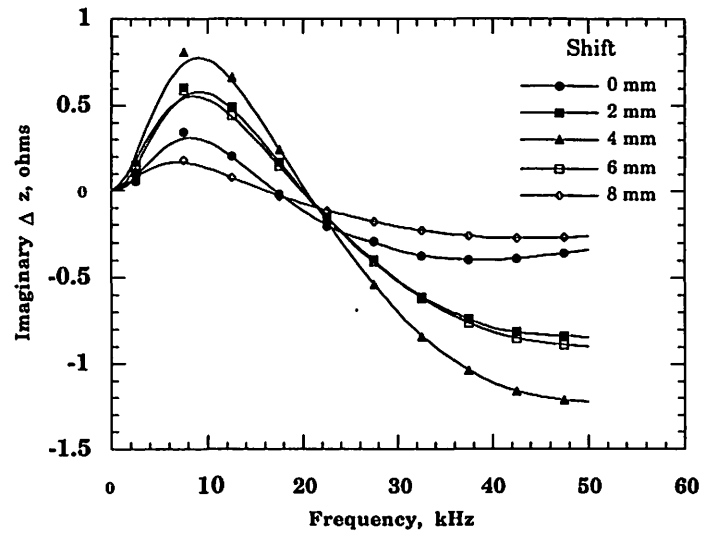
Figure 5.4: Line scan of the real and imaginary impedance change for various offsets of the coils's center from the center of the flat bottom hole.

5.4 Volume Element Calculations

Calculations of the impedance change were coded and carried out by Bing Wang using the volume integral method (VIM). The basic computation involves solving a large matrix for the unknown electrical fields. The implementation used here had the following features. First, the plate geometry required the use of the Greens function for a flat rectangular metal plate. The Greens function was programmed based on the formulas of Weaver[13]. Second, the large size of the flat bottom hole precluded the use of a simple cubic mesh. The resulting



(a)



(b)

Figure 5.5: Change of impedance as a function of eddy-current frequency

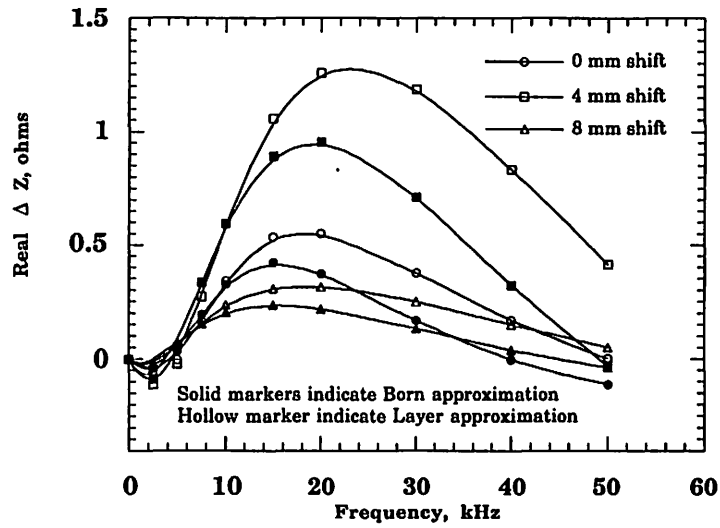
matrix is too large for storage. Consequently, a novel Wavelet basis was used[14], which has the effect of concentrating the elements where the field is rapidly varying and thus reducing the size of the resulting matrix.

Third, thresh-holding was used to set matrix elements less than 0.005 times the largest element in the array equal to zero. This reduces the number of matrix elements that must be held in storage at any one time. Here we make use of the volume integral calculations to test the credibility of the layer approximation.

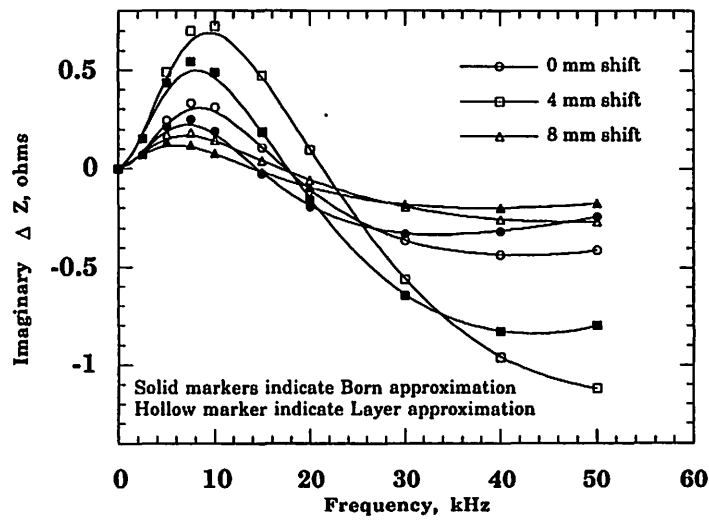
Calculations using the volume integral method were made for the benchmark problem as a function of both frequency and as a function of the offset between the center of the defect and the center of the coil. The same calculations were also completed for a second related sample (the two layer sample), whose geometry and results are discussed in chapter six. This sample, which mimics the lap-joint geometry, consists of two 1 mm plates of aluminum with a right-cylindrical hole at the bottom of the top plate. The results for the two layer case are presented in chapter six. The more exact volume element method was in good agreement with the layer approximation for both the cases as will be seen in later sections. The volume integral method is computationally expensive and is difficult to implement for large defect dimensions.

5.5 Comparison of Layer Approximation and Born Approximation

Figures. 5.6a and 5.6b compare the two different perturbation approximations, namely the layer approximation and the Born approximation. The Born approximation gives smaller values for the change of impedance. As we shall see in the next section, the results of the layer approximation agree very well with both experiment and a more exact theoretical method called the volume integral method. This implies that the layer approximation is better than the



(a)



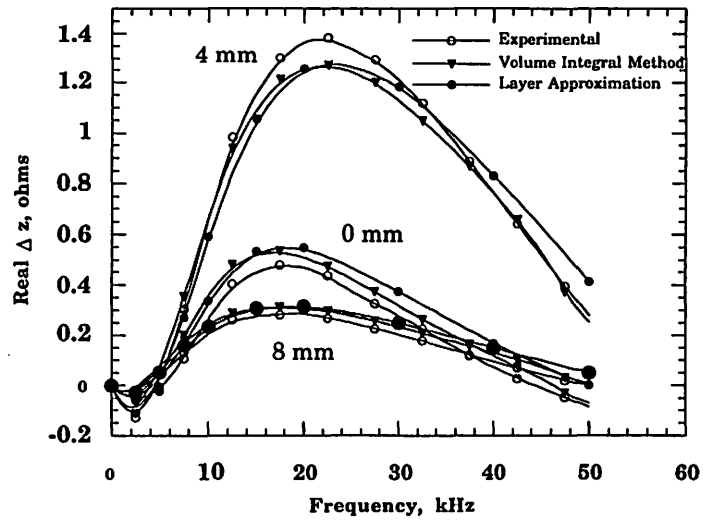
(b)

Figure 5.6: Comparison of layer approximation and Born approximation

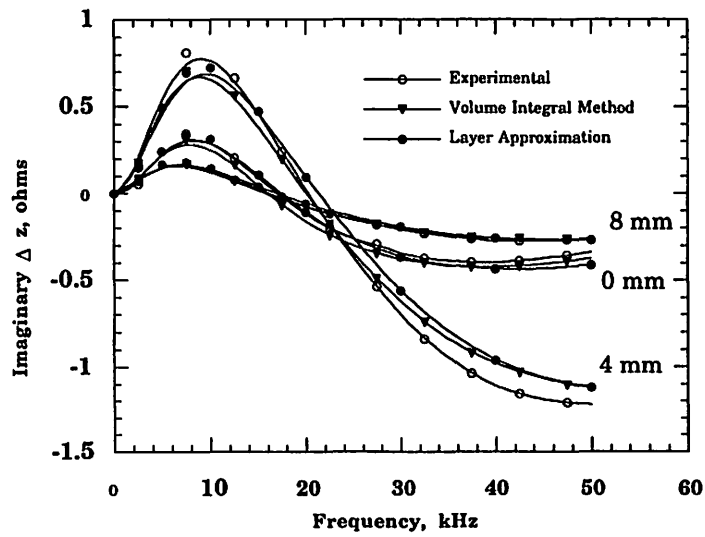
Born approximation. The reason for the disagreement is that the Born approximation is good only for flaws whose conductivity is close to that of the layer. We can conclude that the agreement is not good and this illustrates the shortcomings of the Born approximation in this particular case. This implies that the Born approximation is seriously limited by the defect dimensions and the nature of the defect (defect conductivity).

5.6 Comparison of Layer Approximation, VIM and Experiment

Figure. 5.7a compares the layer approximation, the VIM calculations and the experimental measurements for the change in the real part of the impedance as a function of frequency for offsets of 0, 4 and 8 mm for the benchmark problem. Figure. 5.7b presents the same comparison for the change in the imaginary part of the impedance. All methods show the same qualitative features. Furthermore, the layer approximation is in good quantitative agreement with the VIM and experiment. This agreement is gratifying and suggests that the layer approximation is a good solution to the actual problem. It demonstrates the power and simplicity of perturbation methods to solve difficult problems. This implies that the layer approximation can indeed be a useful tool to solve industrial problems. The application of the layer approximation to a range of problems pertaining the industry is dealt in the next chapter.



(a)



(b)

Figure 5.7: Comparison of layer approximation, VIM and Experiment

6. PERTURBATION RESULTS FOR VARIOUS CANONICAL PROBLEMS

The layer approximation has been used to compute the impedance for a several problems of interest. In section 6.1, we model the occurrence of pitting corrosion in a lap-joint. In section. 6.2 we model the impedance change introduced by a rivet in a lap-joint. In section. 6.3, we model the rippled interface between a thin metal surface layer and a metal substrate. Finally, in section 6.4, we treat the case of a subsurface inclusion in a thick metal plate.

6.1 Pitting Corrosion in a Lap-joint

Two 1 mm thick sheets of 2024 aluminum, one plate laid flat on top of the other as shown in Figure. 6.1, are used to model a lap-joint. The conductivity of the sheets was assumed to be uniform and 1.85×10^7 S/m. A flat bottom hole with a nominal radius of 3 mm and a nominal depth of 0.275 mm was drilled in the bottom of the top plate. This example simulates the case of hidden corrosion in lap-slices and has significant practical application, especially for corrosion detection in aircraft. Figure. 6.2 shows the conductor geometries for the actual case, the reference case and the layer approximation. Figure 6.3 a,b show the result of the layer approximation and the VIM calculation for the real and imaginary parts of the impedance change as a function of frequency for several different offsets. Qualitatively, the shape of the curves is very similar to that observed for the single layer benchmark sample (Figure 5.7 a,b); the major difference is that the signals are reduced by approximately a factor

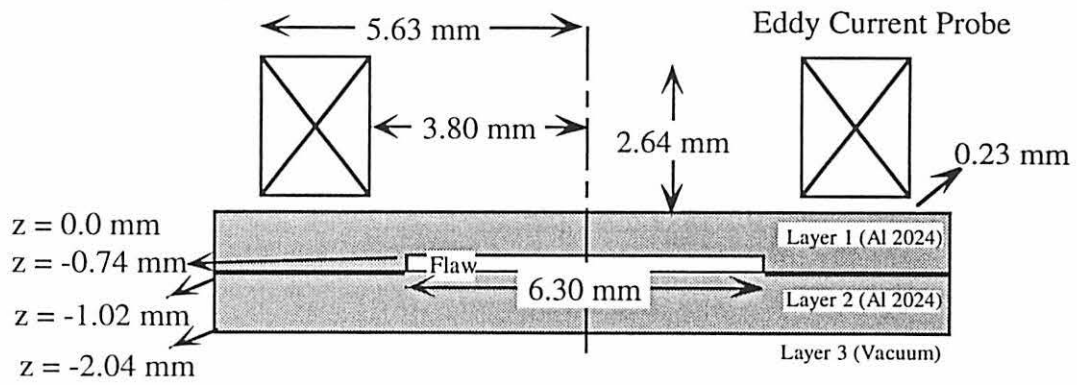


Figure 6.1: Pitting corrosion in a lap joint

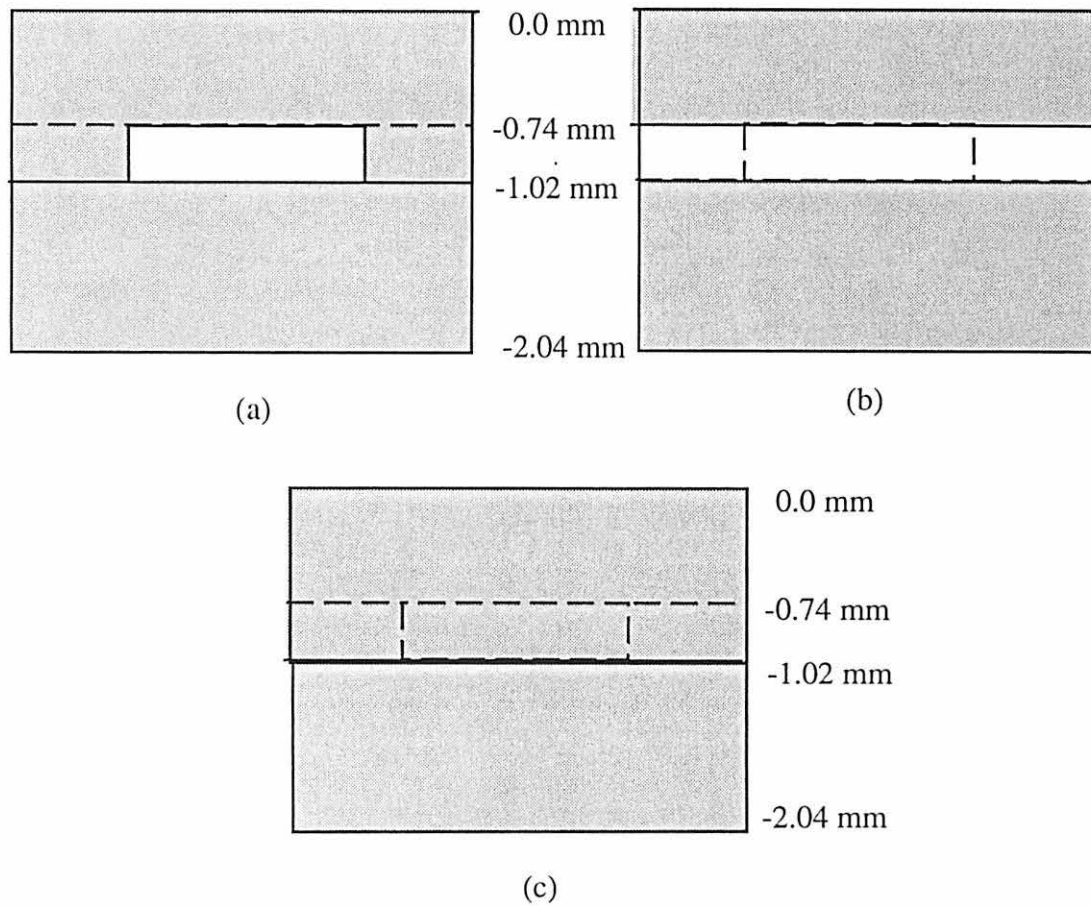
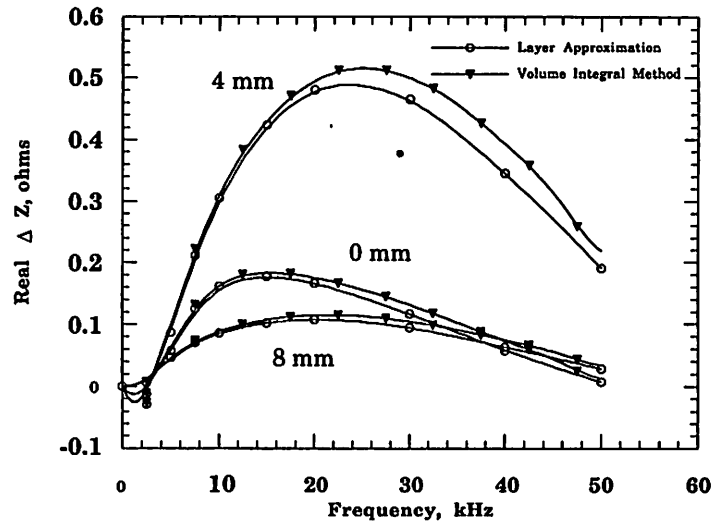
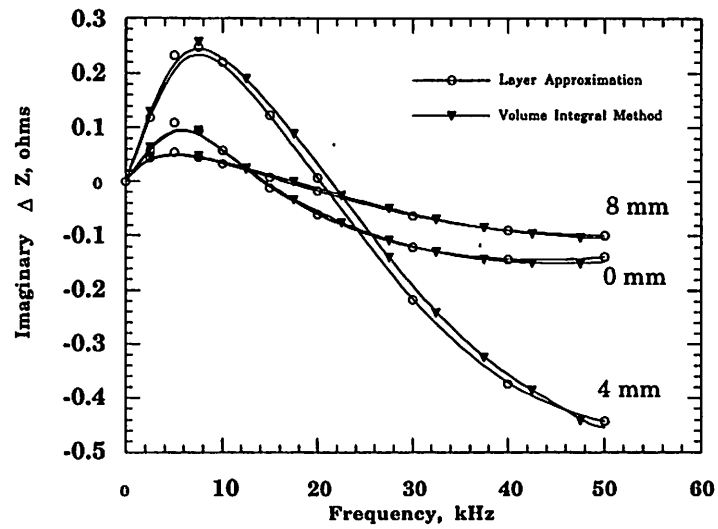


Figure 6.2: Layer conductor geometry for lap Joint
 (a) Actual case
 (b) Layer approximation
 (c) Reference case ^a

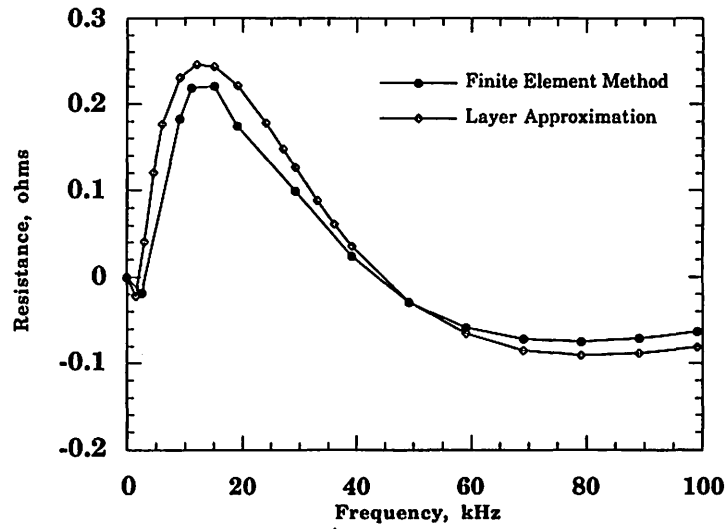


(a)

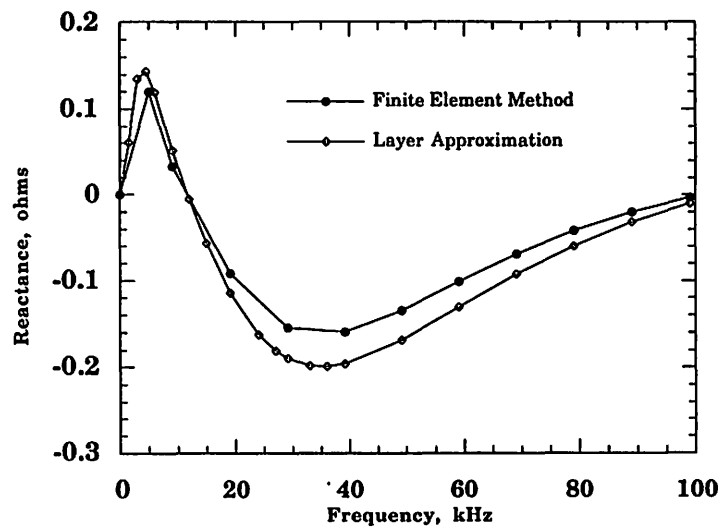


(b)

Figure 6.3: Comparison of layer approximation and VIM



(a)



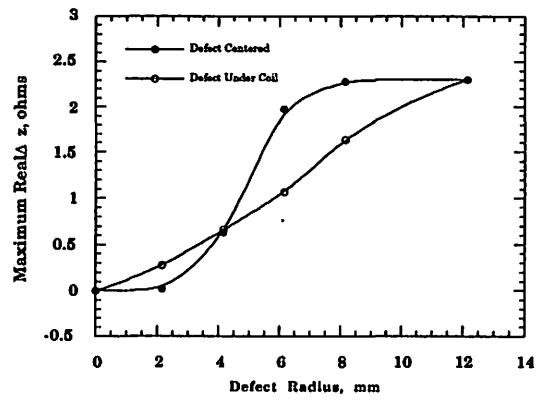
(b)

Figure 6.4: Comparison of layer approximation and FEM

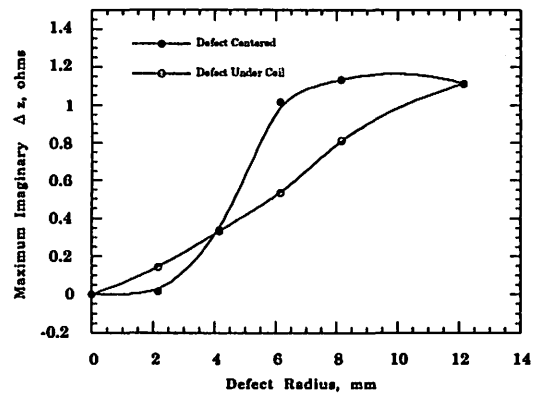
of two for the two layer lap-joint geometry. The impedance changes predicted by the layer approximation are, as can be seen, in good quantitative agreement with the numerically-exact VIM. The layer approximation is also compared with results obtained through another theoretical method, the finite element method (FEM). Results are shown in Figures 6.4 a,b. This comparison was for a second case of aluminum alloy with conductivity 2.88×10^7 S/m. The defect depth was 16 mils and the defect radius was 6.3 mm. The agreement of the layer approximation and the finite element method was good. Our results suggest that the layer approximation will be useful for modeling pitting corrosion in aircraft lap-joints. Next we consider the effect of different parameters such as defect radius, defect depth, layer conductivity and the shift of the defect from the center of the coil on the change in impedance. Before doing so, we consider the maximum change in the impedance because this is the criterion that dictates the size of a detectable defect.

6.1.1 Maximum Signal

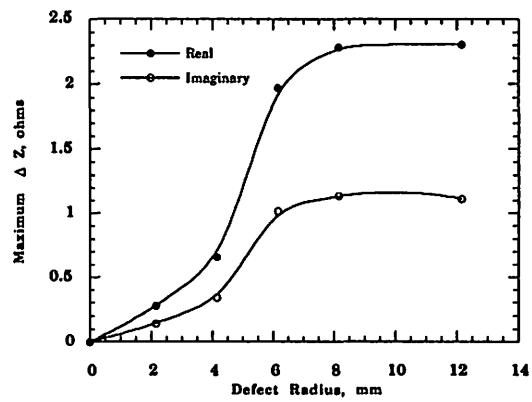
The maximum impedance change observed for a given coil and flat bottom hole is of considerable interest. The layer approximation was used to compute the impedance change for a number of flat bottom holes of differing radii and with a depth of 0.275 mm. For each radius, we found that frequency (≈ 20 kHz) for which the signal is a maximum. Figures 6.5 a,b show the real and imaginary parts of the maximum impedance change as a function of the radius. The maximum values for the case when the defect was located at the center of eddy-current coil, as well as directly under the coil, are shown. For radii less than 4 mm, the signal increases nearly linearly with radius. There is a break in the slope of the curve at 4 mm and the magnitude of the maximum signal then increases rapidly until the radius of the flat bottom holes reaches 6 to 7 mm. For larger radii, the maximum strength of the signal is constant. For small radii (< 4 mm), the signal is a maximum when the hole is directly below the wires



(a)



(b)



(c)

Figure 6.5: Maximum impedance change as function of defect depth

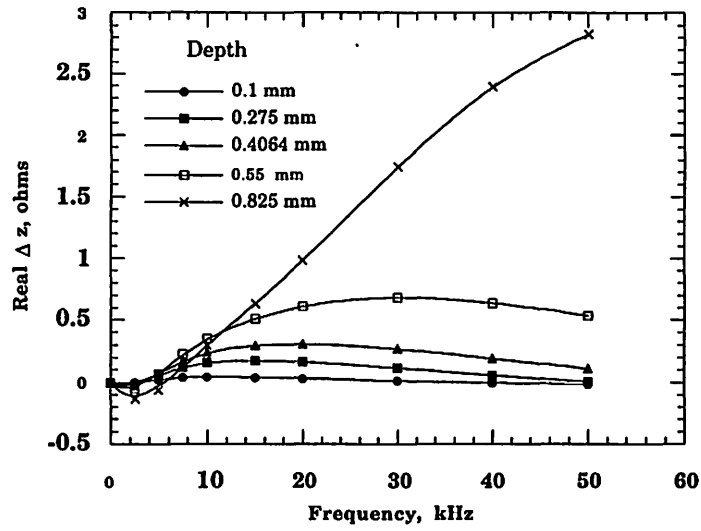
that constitute the coil. For larger radii (>4 mm) the signal is a maximum, when the holes is centered with respect to the axis of the coil. The plot showing the maximum real and imaginary parts of the change in impedance, irrespective of whether the defect is centered or under the coil is shown in Figure 6.5c.

6.1.2 Effect of Defect Depth

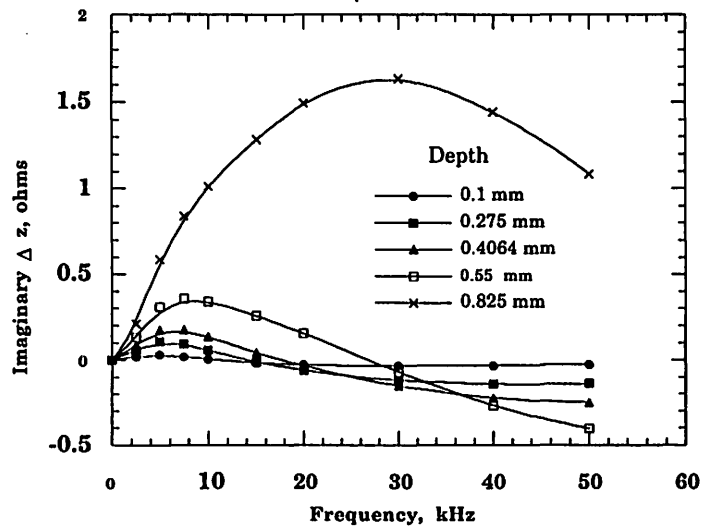
We have also calculated the impedance change for a flat bottom hole of fixed radius (~ 3 mm) as a function of the depth of the hole. The defect depth was varied from 0.1 mm to 0.825 mm. The general shape of the change in impedance curve plotted as a function of frequency is similar for all defect depths as seen from Figures 6.6 a,b. Though the curve corresponding to defect depth of 0.825 mm appears to be of a different shape, the curve approaches zero at frequencies that are higher than those shown in the plots and hence assumes the same shape. The change in impedance is also plotted as a function of defect depth in Figures 6.7 a,b,c,d. The real and imaginary plots for frequencies less than 15 kHz and greater than 15 kHz are plotted separately for clarity. Figure 6.8 shows the magnitude of the change of impedance as a function of defect depth. As expected, the magnitude of impedance change increases with increasing depth.

6.1.3 Effect of Defect Radius

The effect of defect radius on the change in impedance has been studied for two different cases: 1) when the defect is located in the center of the coil and 2) when the defect is positioned directly beneath wires that constitute the coil. The defect radius was varied from 1.15 mm to 12.15 mm. Figures 6.9 a,b show the real and imaginary part of the change in impedance as a function of frequency when the defect is centered. Figures 6.9 c,d illustrate the same when the defect is beneath the coil. The change in impedance is much larger when the defect is beneath the coil due to a stronger electric field in that region. The change in

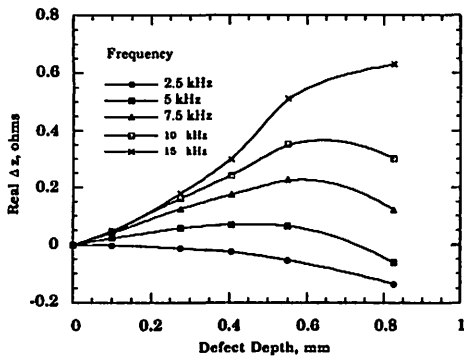


(a)

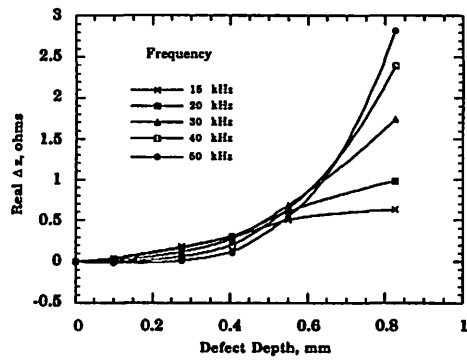


(b)

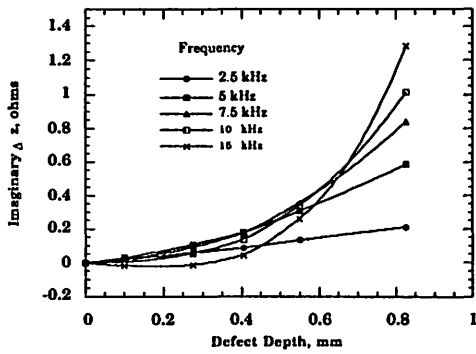
Figure 6.6: Change of impedance as function of frequency for various depths



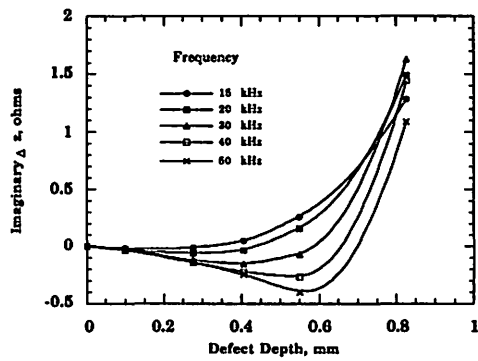
(a)



(b)



(c)



(d)

Figure 6.7: Change of impedance as a function of defect depth

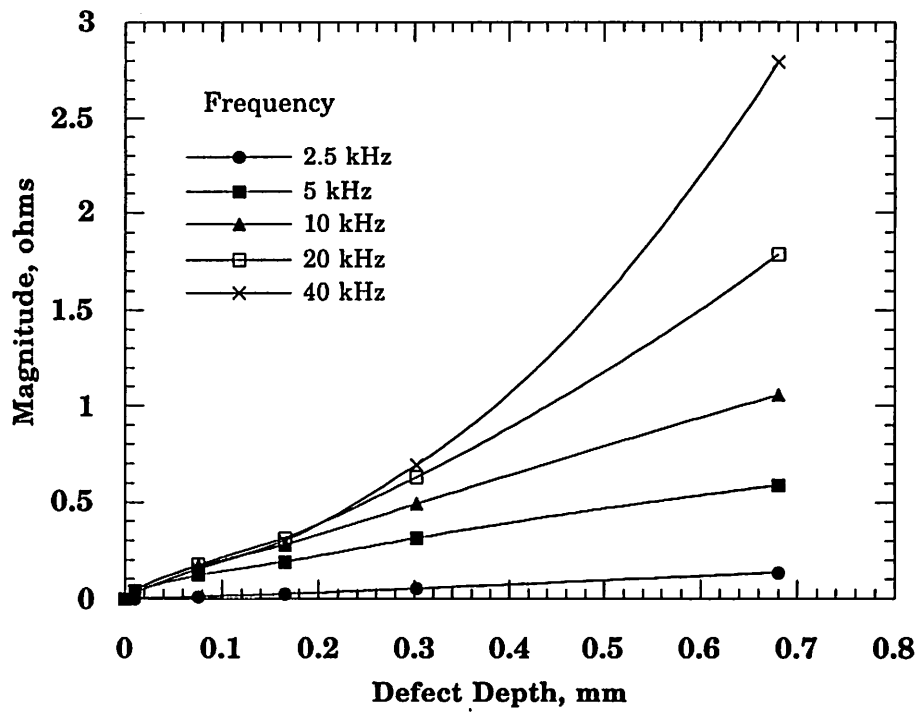
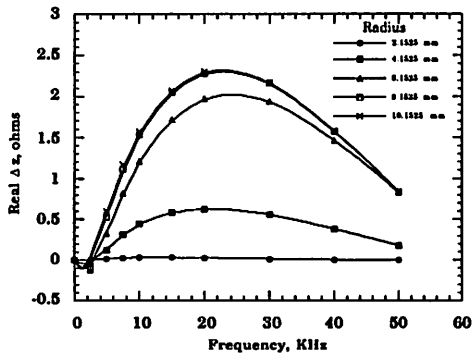


Figure 6.8: Magnitude of impedance change as a function of defect depth

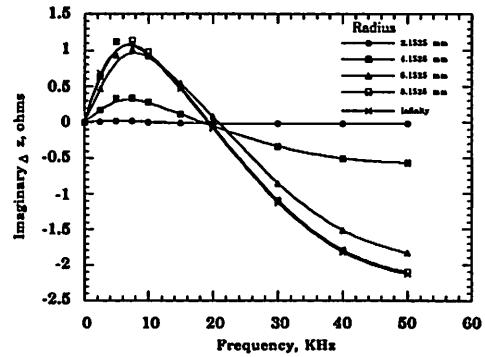
impedance curves approach the curve with large defect radius (close to infinity). For the centered defect case, all the curves corresponding to radius greater than 8.1525 mm were hard to distinguish. The critical radius when the defect is beneath the coil is greater and is around 12 mm. We tried scaling these change in impedance curves to one, in order to check if the curves only differed by a constant multiplication factor and would coincide. The effect of scaling when the defect was centered was disappointing as can be seen from Figures 6.10 a,b. However, when the defect was located directly beneath the coil, all the curves corresponding to different radius overlapped when scaled to one (Figures 6.10 c,d). This is a very interesting result and can be of advantage to the industry as a number of unnecessary calculations at different frequencies can be eliminated once the scale factor is known. Another problem of interest is the effect of defect volume (corresponding to different defect radius but constant defect height) on the change of impedance. The curves corresponding to defect volume vs. change in impedance appear to have two different slopes when the defect is centered as can be seen in Figures 6.11 a,b. The change in impedance is nearly proportional to the defect volume when the defect is located under the coil as shown in Figure 6.11 c,d.

6.1.4 Effect of Layer Conductivity

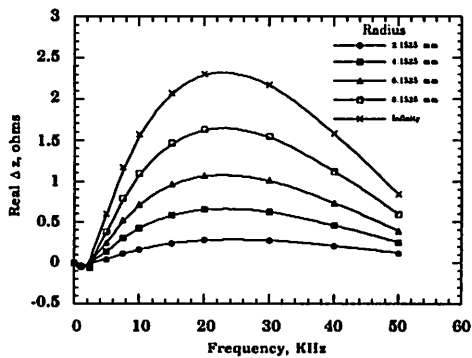
We considered the effect of the conductivity of the plates constituting the layered metal structure on the change in impedance. The two layer sample with a flaw of fixed dimensions (Defect Depth - 0.275 mm, Defect Radius - 3.1525 mm) was taken as a reference. The conductivities of the plates varied from 0.588×10^6 S/m to 5.8×10^7 S/m. The effect of conductivity on the change in impedance was complicated and interesting. The change in impedance showed an unexplained behavior when plotted with respect to the layer conductivity as shown in Figures 6.12 a,b,c,d. This behavior requires a more thorough investigation and is a topic for further research.



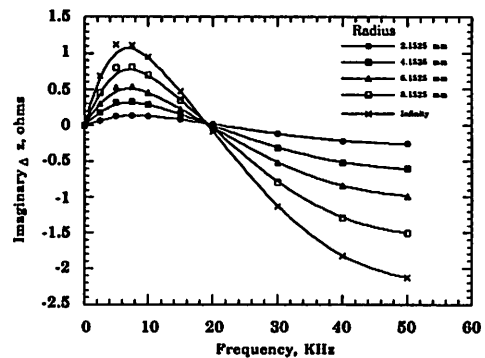
(a)



(b)

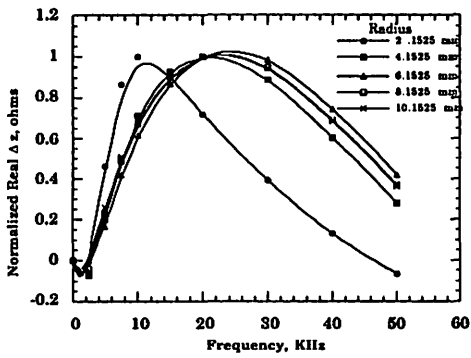


(c)

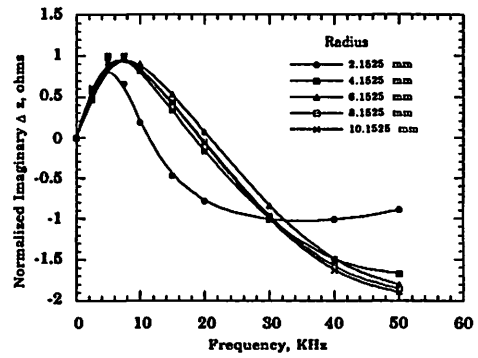


(d)

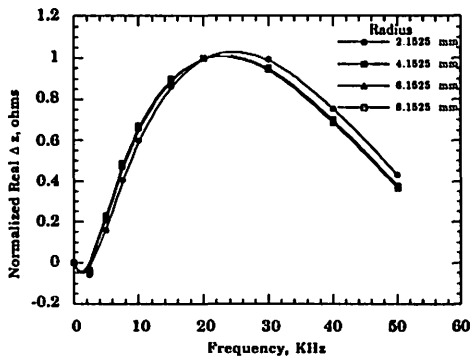
Figure 6.9: Change of impedance as a function of frequency for various defect radii



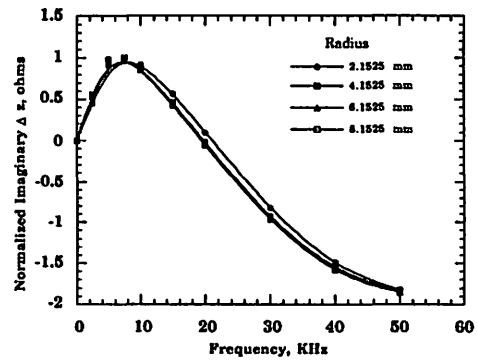
(a)



(b)

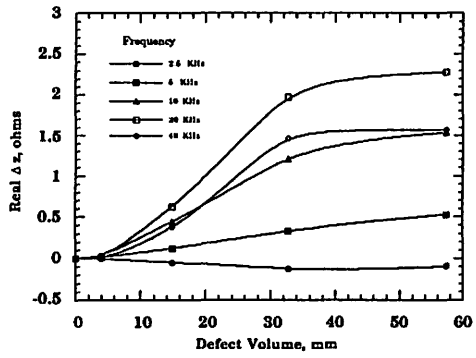


(c)

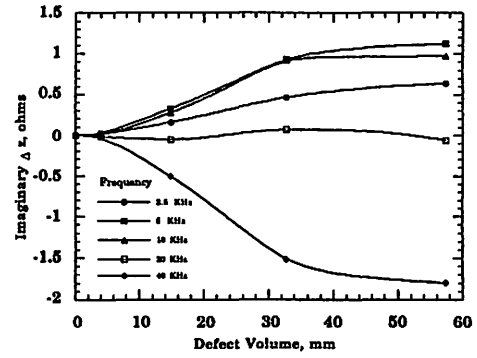


(d)

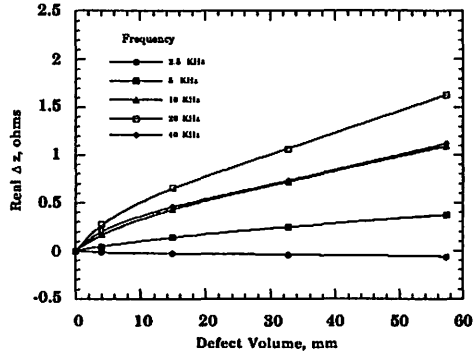
Figure 6.10: Normalized change of impedance as a function of frequency



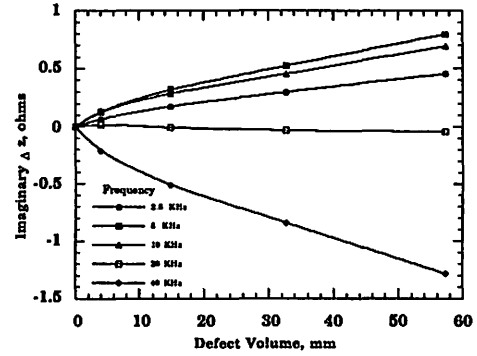
(a)



(b)

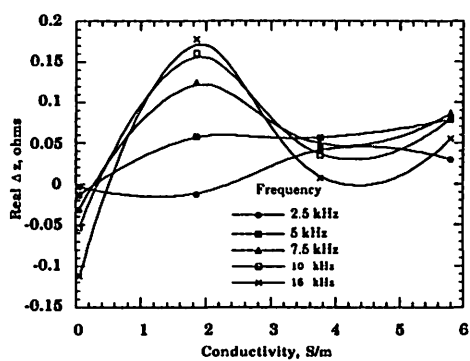


(c)

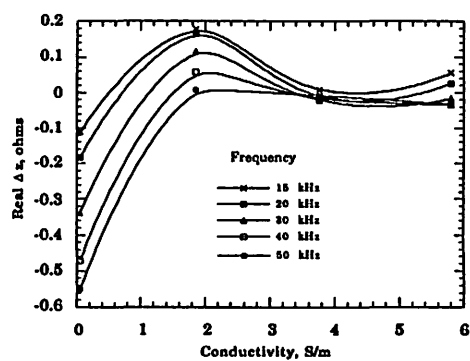


(d)

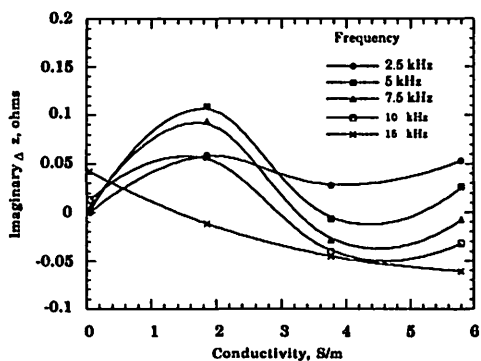
Figure 6.11: Effect of defect volume on change of impedance



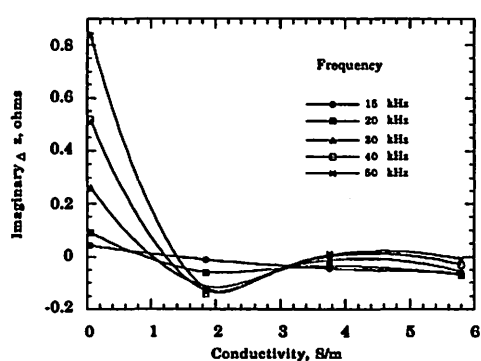
(a)



(b)

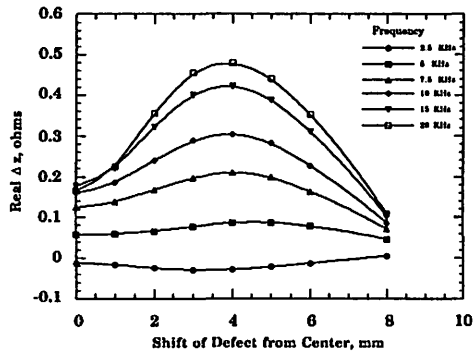


(c)

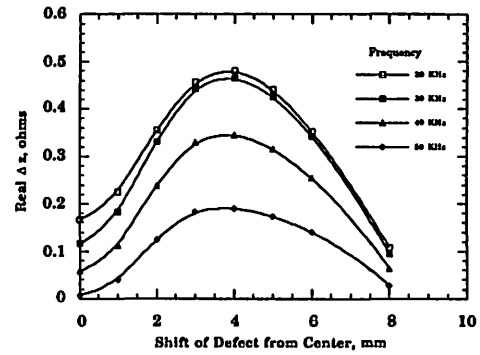


(d)

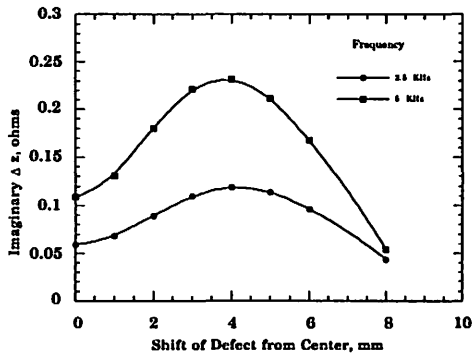
Figure 6.12: Effect of conductivity on change of impedance



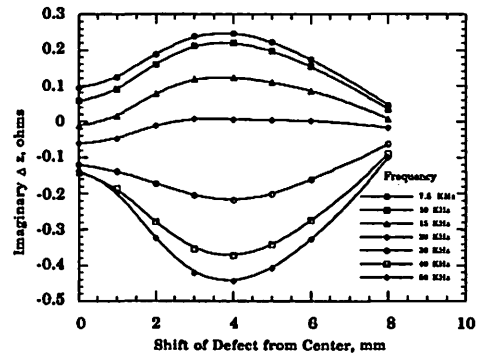
(a)



(b)



(c)



(d)

Figure 6.13: Effect of defect offset on change of impedance

6.1.5 Effect of Defect Offset

The effect of the defect position with respect to eddy-current probe is considered in this sub-section. The change in impedance was calculated when the defect was shifted from 0 mm to 12 mm from the center of the probe. As shown in Figure 6.13 a,b,c,d the real and imaginary parts of the impedance changes increased when the wires that constitute the coil were located near the center of the defect, reaching a maximum at an offset of 4 mm. Finally, the real and imaginary parts of the impedance changes decreased and reached a relative minimum when the coil was centered with respect to the defect. The signal is cylindrical symmetric, since the probe and defect are also cylindrical symmetric. The current induced in the metal (and the degree to which this current is diverted by the defect) is the key to understanding the shape of the plot. The induced current has the shape of a ring, with the current being strongest directly beneath the wires that constitute the coil (i.e. at 4 mm). The induced current is zero at the center of the coil (by symmetry). The induced current also decays to zero far away from the coil. Consequently, the signal was small when the defect was either centered in the coil or is far from the coil. The signal was the maximum when the defect was immediately beneath the wires.

6.2 Rivet in a Lap Joint

A schematic cross-section of a cylindrical rivet in a lap joint is shown in Figure 6.14. The rivet is a surface breaking inclusion of foreign metal that ties together sheets of 1 mm 2024 aluminum alloy. In order to simulate the rivet, we have assumed that the rivet is made of an aluminum alloy that is harder than the 2024 alloy that constitutes the plates. Increased hardness can be achieved by introducing impurities and atomistic defects. Consequently, we supposed that the conductivity of the rivet was less than that of the 2024 alloy. We arbitrarily assumed that the conductivity of the rivet was 1.57 S/m , 85% of the conductivity of 2024

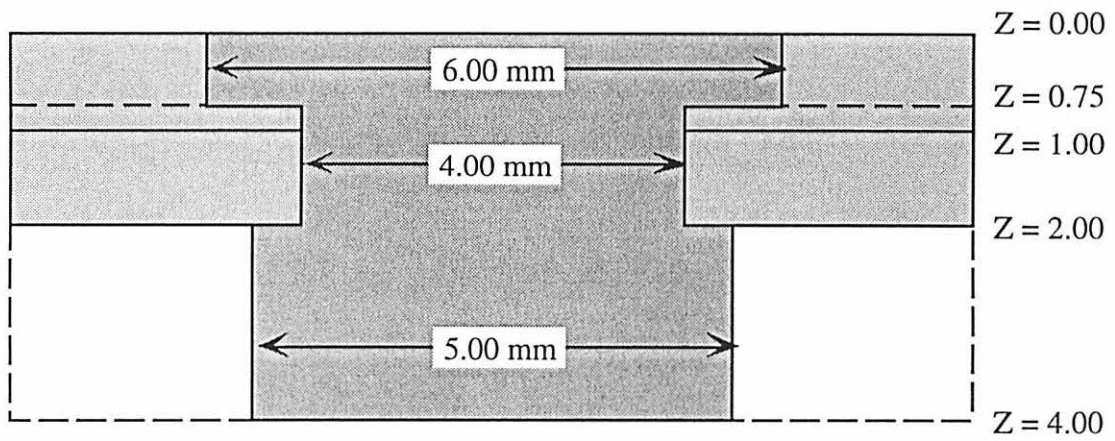


Figure 6.14: Rivet in a lap Joint

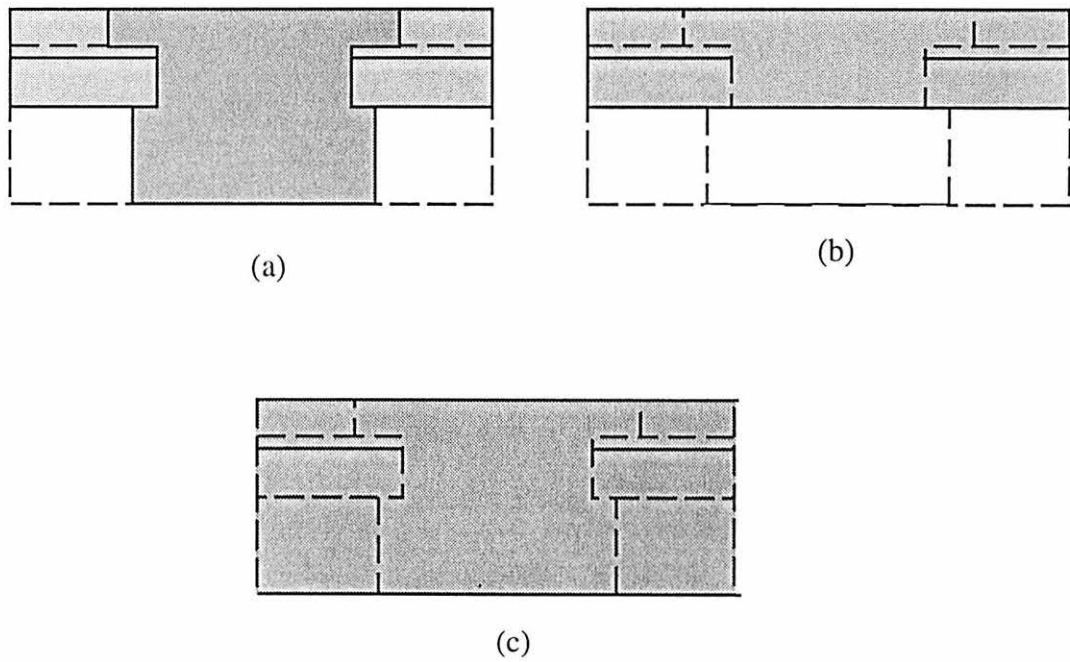
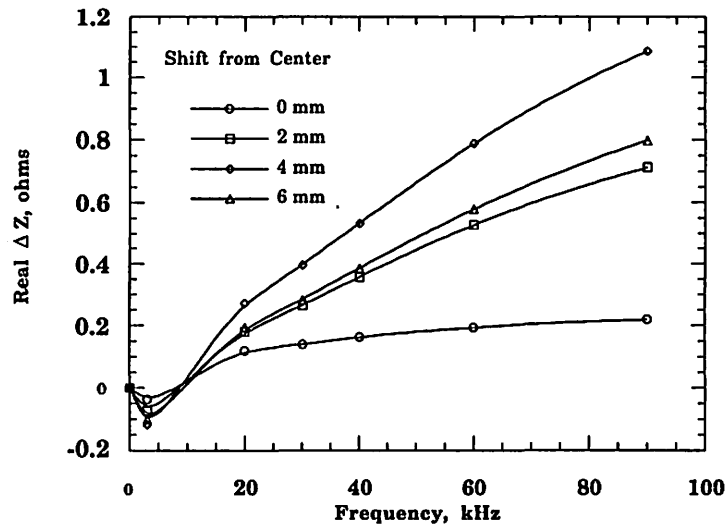
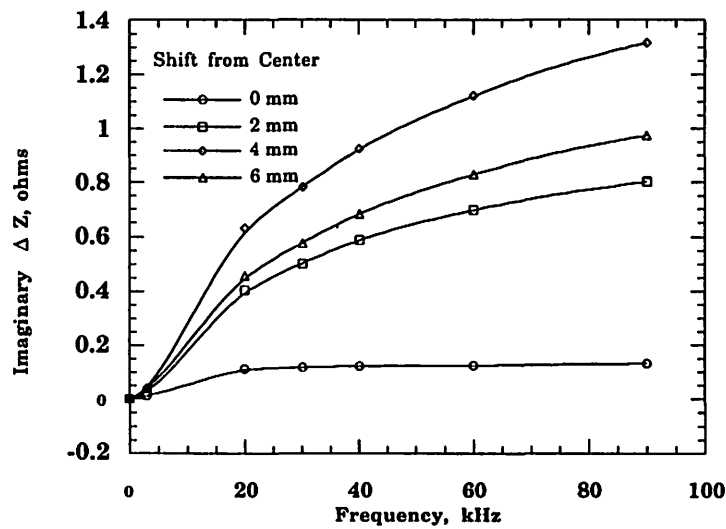


Figure 6.15: Conductor geometry
 (a) Actual case
 (b) Reference case
 (c) Layer approximation

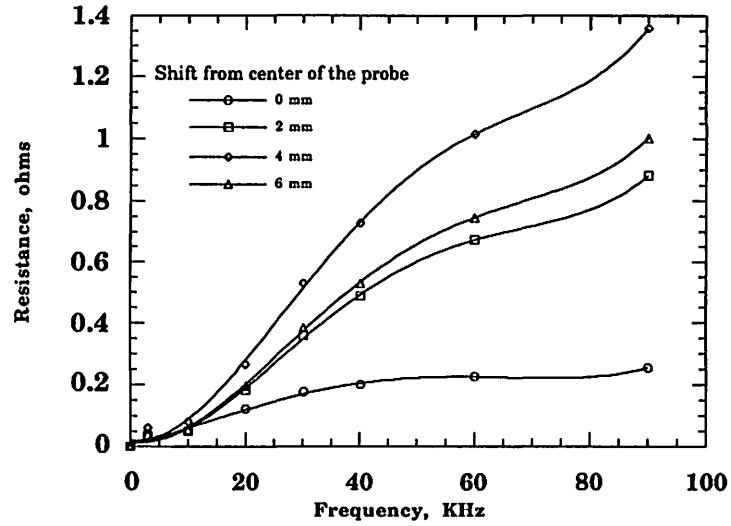


(a)

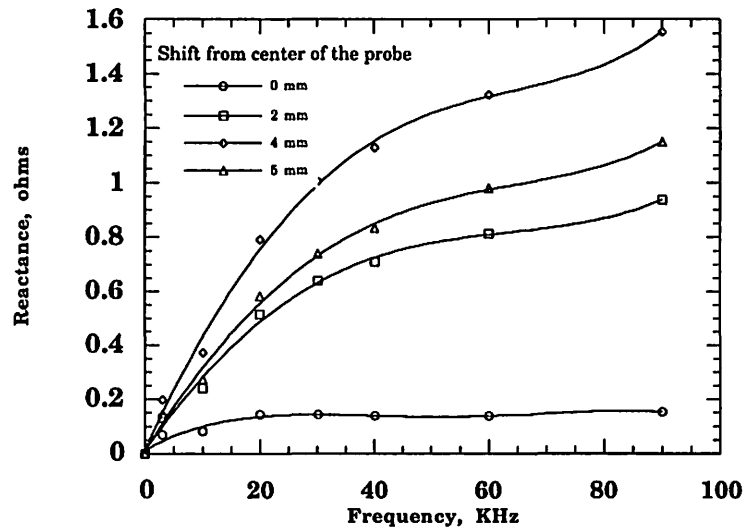


(b)

Figure 6.16: Change in impedance due to presence of rivet
(Conductivity of rivet is less than the layer)



(a)



(b)

Figure 6.17: Change in impedance due to presence of rivet
(Conductivity of rivet is greater than layer)

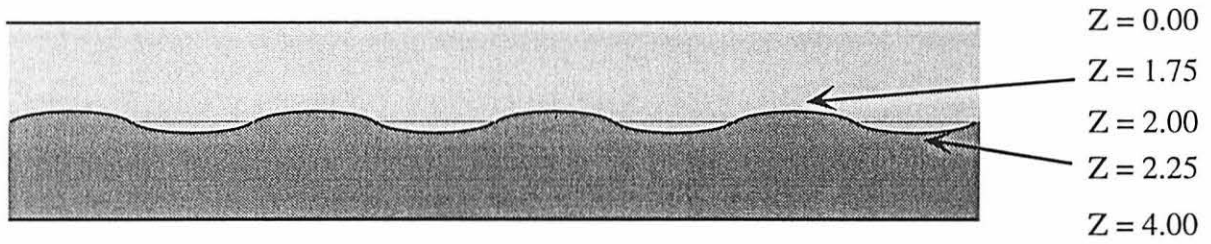
aluminum. The layer approximation, in this case, was based on the calculation of the electric field for the coil above two different plates. First, we computed \bar{E}_0 for the reference, a 1 mm plate of 2024 aluminum with a nominal conductivity of 1.85 S/m. Second, we computed \bar{E}_L for a plate that had a thickness equal to the length of the bolt (4 mm) and a conductivity of 1.57 S/m. The conductor geometries for the reference case, for layer approximation and the actual case of rivet in a lap splice are shown in Figure 6.15 a,b,c.

Figures 6.16 a,b shows the real and imaginary parts of the impedance change as a function of frequency for a variety of distances between the center of the coil and the center of the rivet. The signal is small at low frequencies and then increases monotonically with frequency. At 20 kHz the maximum magnitude of the signal from the rivet was found at an offset of 4 mm and is approximately 1 Ohm. Thus, we found that the signal from a rivet interferes significantly with the signal expected from pitting corrosion, which is expected to be in the range of 0.1 - 4.0 Ohms.

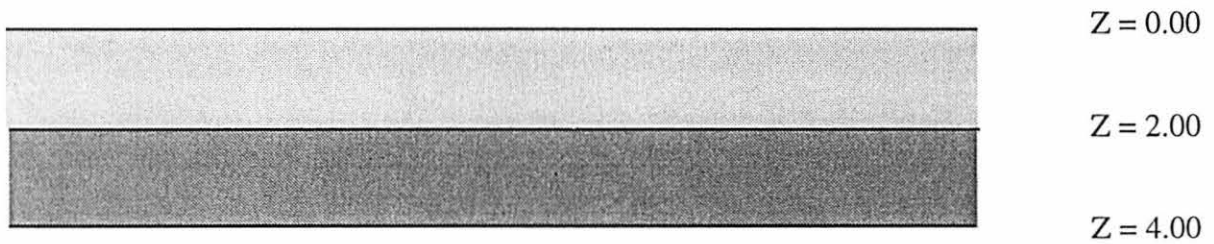
We also analyzed the case of a rivet in lap joint where the conductivity of the rivet was greater than that of the metal plates (about 125%). The conductivity of the rivet in this case was considered to be 2.3e7 S/m. The rest of the details of the conductor geometry are similar to the case where the conductivity of rivet was lower. The results were similar but for a reverse sign as can be seen from Figures 6.17 a,b.

6.3 Rippled Interfaces

The impedance change of a coil next to layered metals that possess rough interfaces is an important and interesting problem that deserves extensive future study. Here, we will broach the topic by considering the sample shown schematically in Figure 6.18. We considered two metal plates joined together at an interface. The interface was assumed to be of sinusoidal nature. The Born approximation results are presented. A layer of aluminum

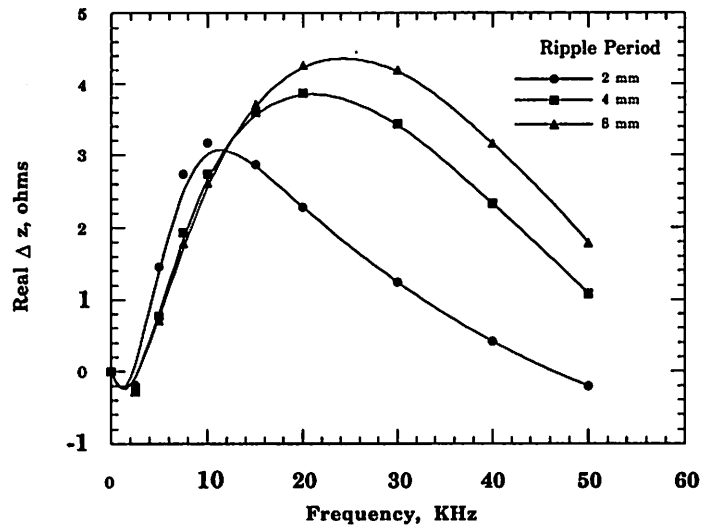


(a)

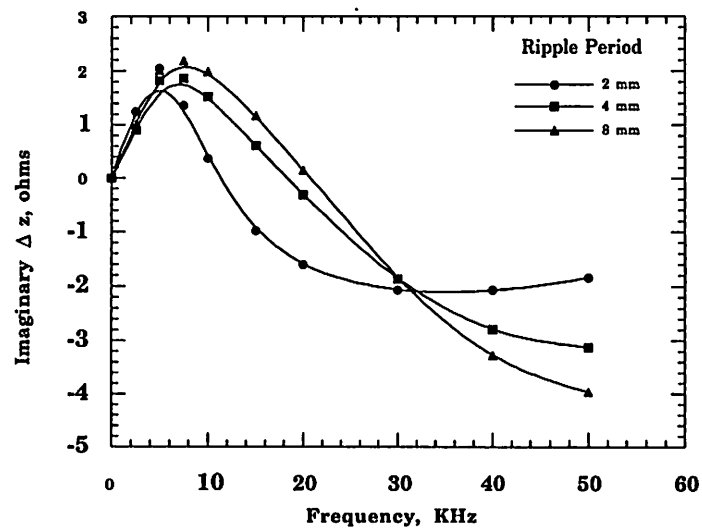


(b)

Figure 6.18: (a) Ripple interface
(b) Reference case



(a)



(b)

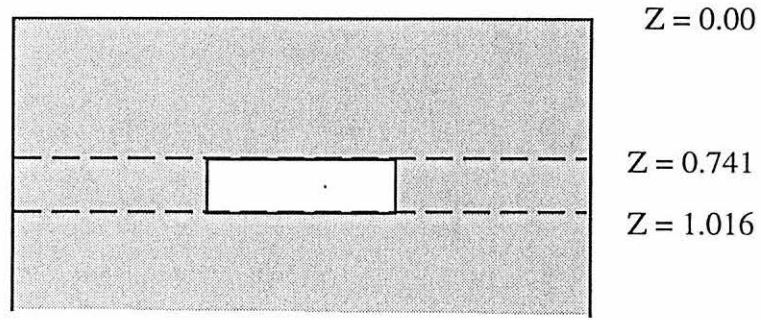
Figure 6.19: Change of impedance for rippled interface

(conductivity - $3.88e7$ S/m) is assumed to be present over a layer of copper (conductivity - $5.8e7$ S/m). Each layer is assumed to be 2 mm in thickness. The amplitude of the ripple is assumed to be 0.5 mm. The wavelength of the ripple is varied from 2 mm to 10 mm. The change in impedance curve followed the general shape when plotted w.r.t. the eddy-current frequency. The ripple wavelength did not effect the amplitude of the change in impedance as seen from Figures 6.19 a,b.

6.4 Subsurface Inclusion

In this section, we consider the effect of a sub-surface inclusion on the change of impedance. A sub-surface inclusion of copper (conductivity - 5.8×10^7 S/m) in stainless steel (conductivity - 0.5×10^7 S/m) is considered as shown in Figure 6.20. The likelihood of copper impurities during casting of stainless steel is the motivation for choosing a copper inclusion in stainless steel. The inclusion is cylindrical with a radius of 3.15 mm and a height of 0.275 mm. The change in impedance curve when plotted w.r.t. frequency showed a change in sign when compared to the case in section 6.1 (Figures 6.21 a,b). This is because the conductivity of the inclusion (copper) is greater than the metal layer in which it is present (as opposed to the case in section 6.1 where the defect conductivity was zero).

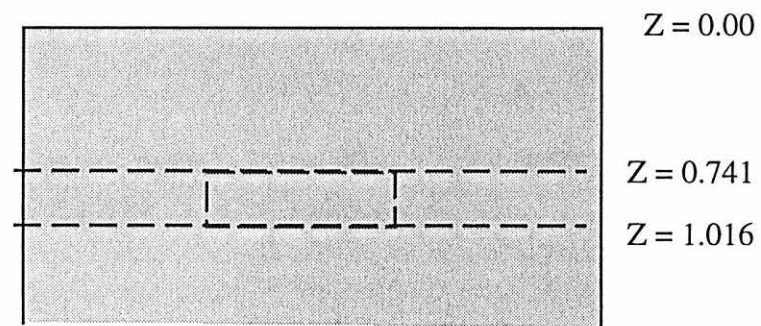
In this chapter we have seen that the layer approximation can be applied to various situations in the industry. The close agreement between the layer approximation and more exact theoretical results is very encouraging.



(a)

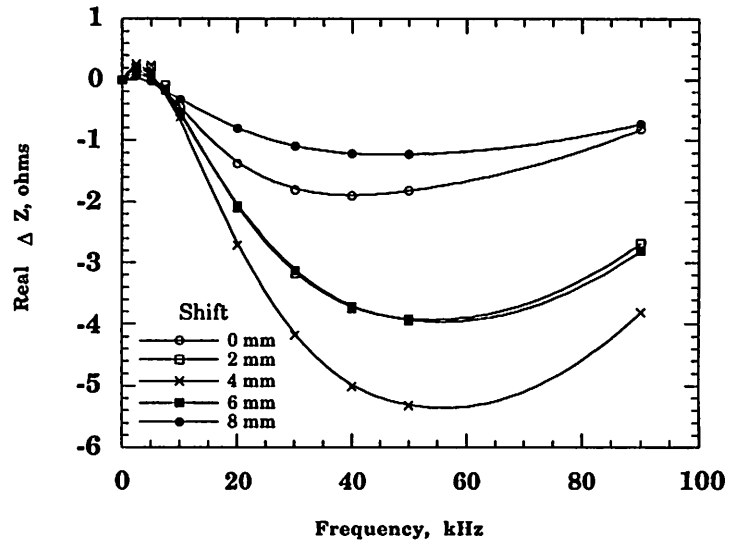


(b)

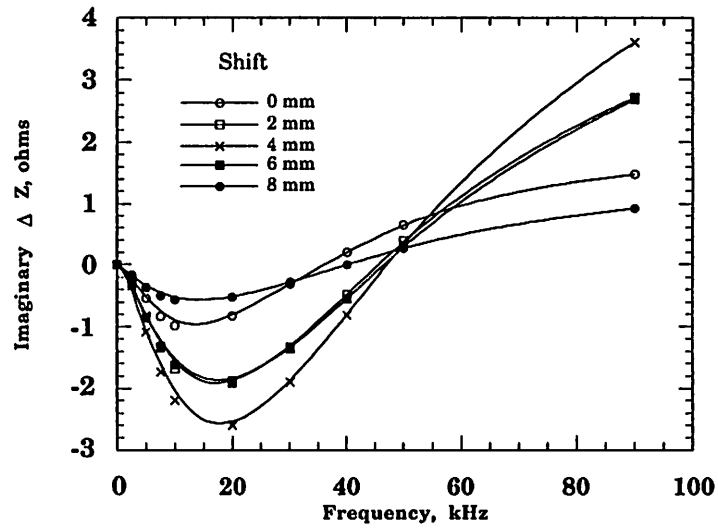


(c)

Figure 6.20: Layer geometry for sub-surface inclusion
 (a) Actual case
 (b) Layer approximation
 (c) Reference case



(a)



(b)

Figure 6.21: Change of impedance due to subsurface inclusion

7. SUMMARY AND CONCLUSIONS

We have developed and presented a new perturbation method (the layer approximation) for the change in impedance induced in a layered metallic structure by a three-dimensional flaw. The layer approximation becomes exact either in the limit that the relative conductivity change approaches zero or in the limit that the flawed region is nearly layered in the neighborhood of the eddy-current probe. The layer approximation was tested for a benchmark problem and in this case agreement between the layer approximation, measurement and more exact theory was excellent. The layer approximation was then used to calculate the impedance change for a number of canonical problems of nondestructive evaluation. The canonical problems were as follows. First, we studied pitting corrosion at the faying surface of a lap joint. Second, we calculated the change in the impedance of a lap joint due to a fastener such as a rivet. Third, we calculated the effects of periodic roughness at the interface between two metallic plates. Finally, we computed the impedance change for a subsurface inclusion in a thick metal plate.

REFERENCES

1. D.E. Hughes, *Phil. Mag.* **8**, 50 (1879).
2. F. Forster and H. Breinfeld, *Z. Metallkunde*, **43**, No. 5, 163-180 (1952).
3. Michael L. Burrows, Ph.D. dissertation, The University of Michigan, Ann Arbor, Michigan (1964).
4. C.V. Dodd and W.E.E. Deeds, *J. Appl. Phys.*, **39**, No. 6, 2829-2838 (1968).
5. C.C. Cheng, C.V. Dodd and W.E. Deeds, *Int. J. Nondestr. Test.*, **1**, 29-90 (1969).
6. S.J. Norton, A.H. Khan and M.L. Mester, *Res. Nondestr. Eval.* **1**, 167 (1989).
7. J.C. Moulder, E. Uzal, and J.H. Rose, *Rev. Sci. Instrum.* **63**, 3455 (1992).
8. E. Uzal, J.C. Moulder, S. Mitra, and J.H. Rose, *J. Appl. Phys.* **74** (3), 2076-2089 (1993).
9. A.J.M. Zaman, C.G. Gardner, and S.A. Long, *J. Nondestr. Eval.*, **3** (1), 37-43 (1982).
10. B. A. Auld, *Eddy Current Characterization of Materials and Structures*, edited by G. Birnbaum and G. Free, ASTM, Philadelphia, 332-347 (1981).
11. B.A. Auld and J.C. Moulder, "Eddy Current Modeling" unpublished.
12. David M. Pozar, "Microwave Engineering." Addison-Wesley Publishing Co., Reading, Massachusetts (1990).

13. J.T. Weaver, *Canadian Journal of Physics*, **45**, 1981-2002 (1967).
14. Bing Wang, John P. Basart and John C. Moulder, "Wavelet expansions in volume integral method of eddy current modeling." unpublished.
15. M.Y. Antimirov, A.A. Kolyshkin and R. Vaillancourt, *J. Nondestr. Eval.*, **10**, 31 (1991).
16. A.A. Kolyshkin and R. Vaillancourt, *J. Appl. Phys.*, **77**, 4903 (1995).

ACKNOWLEDGEMENTS

My sincere thanks are due to my research advisor, James H. Rose, who has been extremely supportive and encouraging through all the phases of the research. I would like to express my thanks to John C. Moulder and Bing Wang for providing us with the experimental data and VIM results respectively. I am grateful to my thesis advisor, Satish S. Udpa, for his cooperation throughout my graduate studies. Finally, I would like to thank my friend, Honey Goel for helping me out with various software.